



Hepburn, L. E., Butler, I. B., Boyce, A. and Schröder, C. (2020) The use of operationally-defined sequential Fe extraction methods for mineralogical applications: a cautionary tale from Mössbauer spectroscopy. *Chemical Geology*, 543, 119584.

There may be differences between this version and the published version. You are advised to consult the publisher's version if you wish to cite from it.

<http://eprints.gla.ac.uk/212625/>

Deposited on: 19 May 2020

Enlighten – Research publications by members of the University of Glasgow
<http://eprints.gla.ac.uk>

1 **The use of operationally-defined sequential Fe extraction methods**
2 **for mineralogical applications: a cautionary tale from Mössbauer**
3 **spectroscopy**

4
5 Laura E. Hepburn^a, Ian B. Butler^b, Adrian Boyce^c, Christian Schröder^a

6
7
8 ^a*Biological and Environmental Sciences, Faculty of Natural Sciences, University of Stirling, Stirling FK9 4LA,*
9 *UK*

10 ^b*Earth and Planetary Science, School of GeoSciences, University of Edinburgh, Edinburgh EH9 3FE, UK*

11 ^c*Scottish Universities Environmental Research Centre, Rankine Avenue, East Kilbride G75 0QF, UK*

12
13
14
15 Corresponding author: Laura E. Hepburn

16 Email: leh1g09@soton.ac.uk

17
18
19
20
21 **Submitted to *Chemical Geology***

22 **September 2019**

23
24
25 Declarations of interest: none

29 **Abstract**

30 Reactive iron minerals are crucial components of global nutrient cycles, directly controlling
31 carbon transport and storage in marine sediments. Sequential selective extraction is
32 frequently used for quantitatively characterising, and chemically isolating, individual Fe
33 mineral phases. Reagent-specific mineral solubility is fundamental to the success of any
34 sequential extraction, but is strongly affected by the varying physical and chemical
35 morphology intrinsic to natural mineral samples. Natural sediment, rock, and soil samples
36 often contain a mineral mixture, which further modifies solvent efficacy. ⁵⁷Fe Mössbauer
37 spectroscopy only probes the hyperfine interactions between next-nearest neighbouring
38 atomic nuclei in the crystal lattice and is less affected by variation in mineral grain size and
39 crystallinity than conventional, X-ray-based methods. In this study, we used Mössbauer
40 spectroscopy in a novel context to cross-calibrate and optimise a popular, but frequently
41 misused, sequential Fe extraction protocol. Our results showed that incomplete and premature
42 removal of the target Fe minerals could occur at nearly every stage of the extraction and, in
43 many cases, the leachate Fe content did not represent the target phase at all. Crystalline,
44 natural siderite and amorphous, synthetic goethite were detected in the Mössbauer spectrum
45 of the ammonium oxalate extraction for magnetite, after which all reactive Fe minerals
46 should have been removed. Consistent with previous studies, and unlike many other clay
47 minerals, nontronite was extracted as part of the highly reactive Fe pool, and in fact our data
48 indicate that this mineral was extracted by the initial Na-acetate extraction that targets
49 'carbonate-bound Fe'. Matrix effects appeared to cause variable yield efficiencies: synthetic
50 goethite was successfully removed when present as an individual mineral yet persisted
51 beyond its target extraction when present in an Fe mineral mixture. Although suitable for the
52 quantification of operationally-defined Fe pools, we caution the unverified use of sequential
53 Fe extraction protocols for mineral specific applications. The application of sequential Fe

54 extractions to define the reactive Fe pools as a paleoredox proxy of depositional conditions
55 appears relatively robust. The premature removal of 2-line ferrihydrite observed in this study
56 (due to the use of the more aggressive Na-acetate extraction for crystalline siderite), does not
57 limit the quantitative use of the sequential Fe extraction in ancient sediments, where such
58 ‘easily reducible’ oxides are unlikely to persist. In contrast, attributing the outcomes of
59 operationally-defined Fe pools to specific Fe minerals is precarious and potentially entirely
60 erroneous. Where Fe mineral specificity or separation is required, we recommend post-
61 extraction validation by another secondary technique. Mössbauer spectroscopy offers such a
62 method that can independently verify extraction stages and assess mineral specificity.

63

64 **Keywords:** colloid; nanoparticle; grain size; semi-quantitative characterisation.

65

66

HIGHLIGHTS

- 67 • The operational nature of sequential chemical extractions is frequently misunderstood when
68 used to identify specific mineral phases, and extraction results are often unverified.
- 69 • The incomplete and premature dissolution of target minerals can occur throughout the Poulton
70 and Canfield (2005) extraction for Fe.
- 71 • Grain size and matrix effects largely control the accuracy and the precision of many extraction
72 stages.
- 73 • The use of Mössbauer spectroscopy (MBS) alongside sequential extractions can provide a
74 means of quantitative Fe mineral identification.
- 75 • MBS can characterise amorphous colloidal and nanoparticulate Fe minerals.

76

1. INTRODUCTION

77
78 An estimated 21.5 ± 8.6 % of organic carbon (OC) sequestered within marine sediments is
79 bound directly to reducible Fe(III) oxides (Lalonde et al., 2012). Typically present as
80 amorphous colloids ($< 1 \mu\text{m}$ diameter) or nanoparticles ($< 0.1 \mu\text{m}$ diameter), the Fe(III)
81 oxides have a high surface area-to-volume ratio. Herein, the term “amorphous” refers to both
82 nanoparticulate and true, non-crystalline phases. The stable Fe:OC complexes that protect OC
83 from degradation in oxic marine sediments over million-year timescales (Estes et al., 2019;
84 Lalonde et al., 2012) are currently attributed to the presence of fine-grained material with a
85 large surface area for adsorption (Keil et al., 1994; Mayer, 1994; Berner, 1970) and,
86 increasingly, the specific mineralogy of the Fe (III) oxides (Barber et al., 2017; Ransom et
87 al., 1998). Mixtures of colloidal and nanoparticulate Fe minerals cannot be characterised by
88 conventional analytical techniques (e.g. XRD, transmission electron microscopy), since the
89 particles are generally too small and lack a sufficiently crystalline structure. Sequential
90 selective leaching protocols that relate chemically-mobilised Fe to specific mineral fractions
91 (Poulton and Canfield, 2005; Haese et al., 1997; Heron et al., 1994; Kostka and Luther, 1994;
92 Raiswell et al., 1994; Wallmann et al., 1993; Afonso and Stumm, 1992; Canfield, 1989), are
93 therefore used to better constrain the Fe mineralogy in modern and ancient sediments.

94 Sequential extraction procedures rely on the selective dissolution of a specific metal-bearing
95 phase by particular reagents. The reagents become increasingly aggressive and less specific
96 as the sequence progresses and the metal content of a sample is separated into “operationally-
97 defined” groups (e.g. acetate-extractable Fe) (Kersten et al., 1997; Gobeil et al., 1995; Ure,
98 1991). However, sequential extraction results are often interpreted as the metal content that is
99 bound to a particular mineral phase (e.g. carbonate-bound Fe), despite the unreliability and
100 non-specificity reported from certain extraction stages (Eiche et al., 2010; Reinhard et al.,
101 2009; Sulkowski and Hirner, 2006; Tlustos et al., 2005; Baeyens et al., 2003; Parat et al.,

102 2003; Sahuquillo et al., 1999). Such interpretations ignore the operational nature of the
103 selective extractions and cannot assume the presence of any particular Fe mineral phase in
104 the leachate. There has been a long-standing concern with the use of unverified extraction
105 results to identify specific minerals, or mineral groups, in modern soils and sediments
106 (Sanchez-Espana et al., 2019; Adamo et al., 2018; Schröder et al., 2016; Hass and Fine, 2010;
107 Sutherland, 2010, Zimmerman and Weindorf, 2010; Bacon and Davidson, 2008; Ryan et al.,
108 2008; Gómez-Ariza et al., 1999; Whalley and Grant, 1994; Kheboian and Bauer, 1987).
109 However, a second, independent analytical method that is capable of characterising
110 amorphous Fe colloids and nanoparticles is not always available.

111 The Poulton and Canfield (2005) sequential extraction procedure for Fe is an accessible
112 technique that uses readily-available equipment and reagents. Since it is also capable of
113 quantitatively processing large sample batches, it is used widely throughout the geochemical
114 discipline. The extraction has been applied to ancient sediments in combination with several
115 other independent proxies, to reconstruct palaeoceanic redox conditions (Hammarlund et al.,
116 2019; Oonk et al., 2018; Raiswell et al., 2011; Reinhard et al., 2009) and constrain the timing
117 of major biological radiations in Earth's evolutionary history (Chen et al., 2015; Dahl et al.,
118 2010; Canfield et al., 2007). In modern sediments, the Poulton and Canfield (2005) method
119 has been used to quantify benthic Fe fluxes in continental shelf margin sediments (Scholz et
120 al., 2014; Homoky et al., 2013; Severmann et al., 2010) and to evaluate the importance of
121 bioavailable Fe released from subglacial sediment sources into the open ocean (Henkel et al.,
122 2018; Markussen et al., 2016; Raiswell et al., 2008). The Fe extraction has helped to establish
123 the fundamental role of Fe in global S (Blonder et al., 2017; Wehrmann et al., 2017), P
124 (Ghaisas et al., 2019; Lenstra et al., 2018; Ding et al., 2016), and C (Ma et al., 2018; Peter
125 and Sobek, 2018; Barber et al., 2017) cycling and sequestration. Further to this, the extraction
126 has been used to define the mechanisms for key nutrient (Li et al., 2018; Kraal et al., 2017;

127 Ma et al., 2017; Dijkstra et al., 2016) and toxic metal (Lynch et al., 2018; Nemati et al., 2009;
 128 Weber et al., 2009) mobilisation in freshwater sediment systems.

129 In their original study, Poulton and Canfield (2005) demonstrated the accurate dissolution of
 130 carbonate-associated Fe (Fe_{CARB} ; including siderite and ankerite), easily reducible Fe oxides
 131 (Fe_{OX1} ; including ferrihydrite and lepidocrocite), reducible oxides (Fe_{OX2} ; including goethite,
 132 haematite, and akaganéite), magnetite, (Fe_{MAG}), poorly-reactive sheet silicate (Fe_{PRS}), pyrite

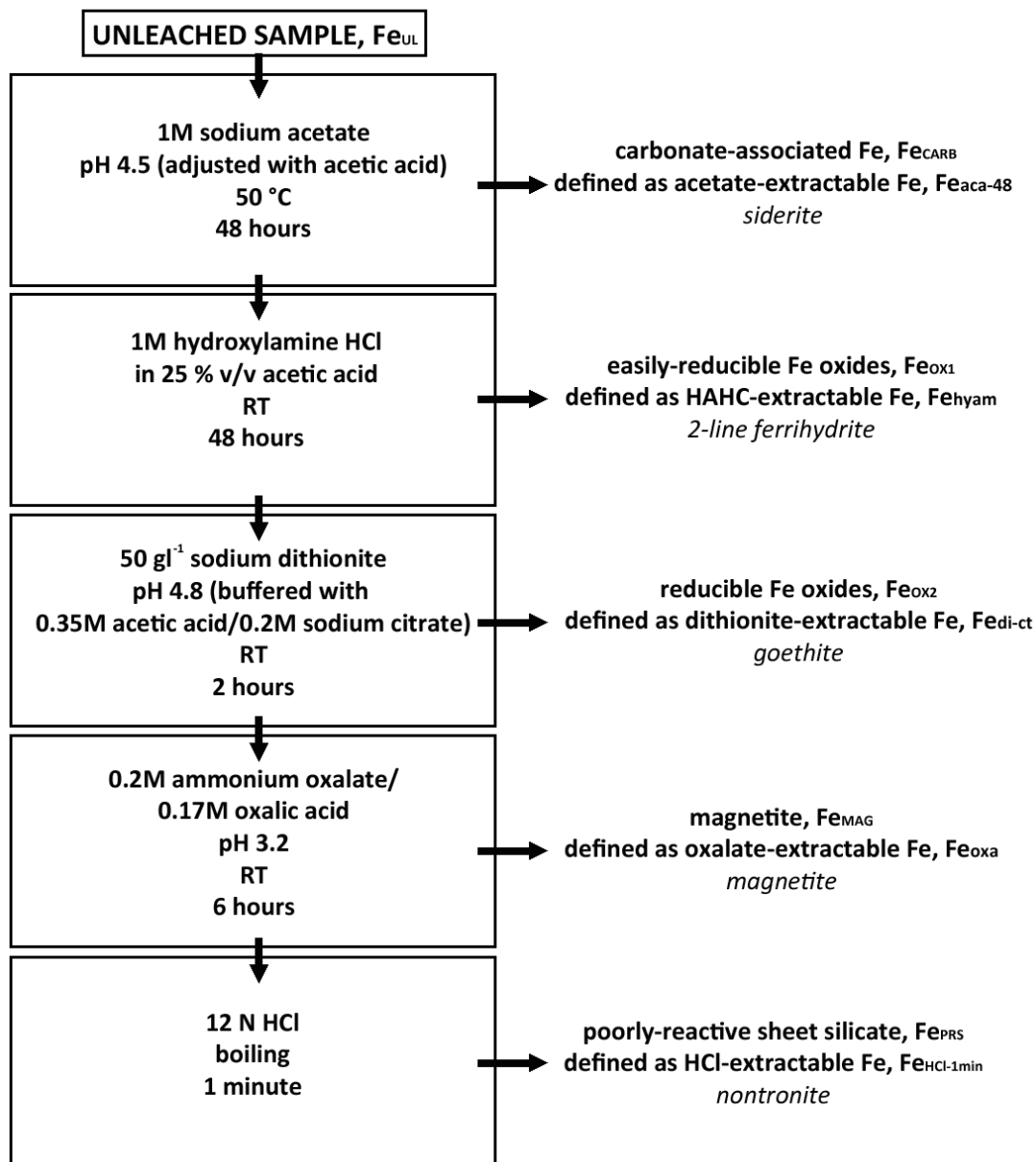


Figure 1: (1.5-column fitting image in black & white) The Poulton and Canfield (2005) sequential extraction procedure for Fe as used in this study. Each extractant is defined to reflect the operational nature of the method, after Henkel et al. (2016, 2018). The mineral selected from each of the “operationally-derived iron pools” defined by Poulton and Canfield (2005), and targeted at each stage in this study, is italicised beneath each labelled extractant. The final $Fe_{HCl-1min}$ does not ‘target’ nontronite, but rather extracts Fe that is poorly reactive towards dissolved sulfide. RT = room temperature.

133 (Fe_{PY}), and unreactive silicate Fe (Fe_{US}) from pure mineral phases. In many subsequent
134 studies, the Poulton and Canfield (2005) sequential extraction for Fe has been applied as a
135 redox indicator, to compare the sum of highly reactive Fe (Fe_{CARB} + Fe_{OXI} + Fe_{MAG} + Fe_{PY})
136 with that of total Fe; in such cases, mineral specific information is not required. However,
137 where sequential extractions are used to discern precise sample mineralogy, it is important
138 that the extraction results are verified.

139 We have combined a modification of the standard Poulton and Canfield (2005) sequential
140 extraction technique (shown in Fig. 1 and explained in detail in Section 2.4) with room
141 temperature ⁵⁷Fe Mössbauer spectroscopy (MBS), to semi-quantitatively verify the specific
142 Fe minerals that are targeted at each extraction stage. MBS probes the hyperfine interactions
143 at the ⁵⁷Fe nucleus between the electromagnetic field of the nucleus, the electromagnetic field
144 of the electron shell, and the electromagnetic field of the crystal lattice. Essentially, MBS
145 utilises a measurement of a mineral directly, rather than the response of a mineral to a
146 chemical reagent and offers a completely independent analytical method. MBS is ideally
147 suited to the identification of reactive Fe minerals in marine sediments because 1) it can
148 individually quantify and characterise different carbonates, iron oxides and oxyhydroxides,
149 sulfides, sulfates, and silicates, and distinguish between the magnetic minerals magnetite and
150 greigite (although the Mössbauer parameter space for certain minerals will overlap); 2) it
151 requires no long range ordering of the crystal lattice, so is capable of analysing crystalline
152 and amorphous colloids, nanoparticles (low temperature measurements are necessary to
153 identify superparamagnetic phases in small particles), and larger phases; 3) it is only sensitive
154 to Fe, any matrix effects caused by more abundant but less reactive mineral phases, e.g.
155 quartz, are blended out; 4) it further determines iron oxidation states, quantifies the
156 distribution of iron between mineral phases and oxidations states, and provides information

157 on the magnetic properties, spin states, coordination, bonding properties, crystallinity, and
158 particle size.

159 MBS has been applied previously to verify individual extraction stages in the sequential
160 Poulton and Canfield (2005) procedure. Following on from experiments simulating
161 Precambrian banded iron formation diagenesis (Posth et al., 2013), the Poulton and Canfield
162 (2005) sequential extraction procedure was used with the intent to extract individual mineral
163 phases for subsequent isotope analysis. Isotope analysis was not carried out because MBS
164 showed that the minerals were not separated as intended. Ferrihydrite was used as a synthetic
165 phase at the start of the experiment discussed by Schröder et al. (2016); lepidocrocite (which
166 is also targeted by the Fe_{hyam} stage) was not present as a starting material and did not form
167 during the high-pressure and high-temperature experiment. After high-pressure and high-
168 temperature treatment, MBS showed unequivocally that no ferrihydrite was present
169 (indicating that all of it had transformed into new minerals), where the sequential extraction
170 suggested the presence of hydroxylamine HCl-extractable Fe oxides (Schröder et al., 2016).
171 The extracted Fe must have come from another, non-target mineral phase. MBS also revealed
172 the presence of siderite beyond its target extraction stage, and the premature removal of
173 magnetite (Schröder et al., 2016).

174 In this study we applied the Poulton and Canfield (2005) procedure, as shown in Fig. 1, to an
175 Fe mineral mixture sediment analogue. We compared the leachate Fe content from each
176 extraction stage with MBS analysis of the residual, leached sediment. We used a suite of
177 natural and laboratory-synthesised Fe minerals to identify the extraction stages in which the
178 target minerals were prematurely or incompletely dissolved. For many of our analyses, we
179 replicated the same synthetic materials that were used to establish the original Poulton and
180 Canfield (2005) method. The use of MBS in this study is not intended as a replacement for
181 sequential selective extraction, rather as a means of testing the extraction method and

182 assessing its suitability for use in different geochemical applications. We have also adopted
183 the extraction stage terminology defined by Henkel et al. (2018, 2016) rather than the original
184 Poulton and Canfield (2005) definitions (Fig. 1), to exemplify the operational nature of the
185 leaching protocol and to avoid misinterpretation of our leach results.

186

187

2. MATERIALS AND METHODS

188 2.1 Fe mineral preparation

189 One target mineral was selected from each of the “operationally-derived iron pools” defined
190 by Poulton and Canfield (2005), excluding exchangeable metals, pyrite and unreactive
191 silicate Fe: Ivigtut (igneous) siderite (for Fe_{CARB}/Fe_{aca-48}), synthetic 2-line ferrihydrite (for
192 Fe_{OX1}/Fe_{hyam}), natural and synthetic goethite (for Fe_{OX2}/Fe_{di-ct}), synthetic magnetite (for
193 Fe_{MAG}/Fe_{oxa}), and two natural nontronite specimens (for $Fe_{PRS}/Fe_{HCl-1min}$) respectively
194 represent the sodium acetate-, hydroxylamine-HCl- (HAHC-), sodium dithionite-, ammonium
195 oxalate-, and HCl-extractable fractions (Fig. 1). It is important to note that the final Fe_{PRS}
196 stage is not mineral specific. Unlike the preceding stages which are designed to target
197 specific operationally-defined mineral groups (Poulton and Canfield, 2005), Fe_{PRS} removes
198 Fe that is poorly reactive towards dissolved sulphide (Raiswell and Canfield, 1996). Raiswell
199 et al. (1994) demonstrated the quantitative extraction of Fe from both oxide/oxyhydroxide
200 and silicate phases using the boiling HCl method of Berner (1970). The use of $Fe_{HCl-1min}$ in
201 this study, is simply to test how effectively it removes the nontronite and any residual Fe
202 mineral phases left behind by the earlier stages. The target minerals were chosen based on
203 their importance in modern sediment studies, ease of MBS identification, and availability.
204 Pyrite is easy to identify using X-ray based techniques and was excluded from this study
205 because it does not face the same issues of characterisation as the more amorphous Fe oxides

206 and oxyhydroxides. Unreactive silicate was also excluded because the bioreactive Fe
207 minerals are the focus of this study.

208 A crystalline sample of siderite from Ivigtut, Greenland, and a powdered sample of natural
209 goethite (unknown locality) were obtained from the teaching collection, School of
210 Geosciences, University of Edinburgh (UK). The natural goethite is hereafter referred to as
211 UoE goethite. The powdered UoE goethite was confirmed as such by reflected light
212 microscopy (before powdering). One natural nontronite (Hungary) sample was kindly
213 donated by the National Museums Scotland Collection Centre (Edinburgh, UK); this sample
214 is henceforth referred to as NMS nontronite. A sample of NAu-2 nontronite, originally
215 collected from Uley Mine, South Australia, was purchased from The Clay Minerals Society
216 (Virginia, U.S.A.). Freshly exposed surfaces of all, natural minerals were selected beneath a
217 hand lens, then ground prior to analysis; the maximum and average grain sizes of each
218 natural mineral are provided in Table 1.

219 Synthetic samples of 2-line ferrihydrite, goethite, and magnetite were prepared from the
220 standard Cornell and Schwertmann (2003) methods, identical to those used to establish the
221 original Poulton and Canfield (2005) method. To synthesise the 2-line ferrihydrite, 500 ml
222 0.1 M iron(III) nitrate was stirred continuously during the addition of 330 ml 1 M potassium
223 hydroxide, until the pH reached 7 – 8. After centrifugation, the suspension was rapidly
224 transferred to sealed sections of dialysis tubing and submerged in ultra-pure H₂O (18.2
225 MΩ.cm) baths at room temperature, to remove electrolytes. 8.5 g of 2-line ferrihydrite was
226 produced by freeze-drying the final, dark red-brown product. Ferrihydrite precipitation was
227 also the first stage involved during goethite synthesis: 180 ml 5 M potassium hydroxide was
228 added to 100 ml 1 M iron(III) nitrate solution. The suspension was diluted to 2 L with ultra-
229 pure H₂O (18.2 MΩ.cm) and sealed in a polypropylene bottle in a preheated, 70 °C oven for
230 60 hours. The final yellow-coloured goethite was then washed repeatedly using vacuum

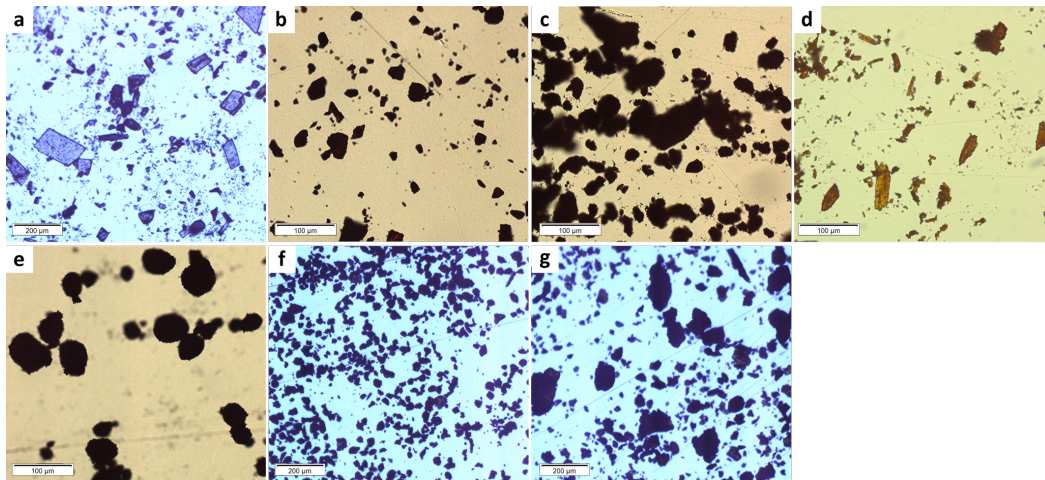
231 filtration and finally dried at 50 °C, to produce approximately 8 g of goethite. For the
232 magnetite synthesis, a 240 ml 3.33 M potassium hydroxide/0.27 M potassium nitrate solution
233 was added dropwise to 560 ml of a 0.3 M iron(II) sulfate solution preheated to 90 °C. All
234 solutions involved in the magnetite synthesis were sparged with N₂ for 2 hours before use.
235 The suspension was heated for a further 60 minutes under constant agitation before the black,
236 magnetite precipitate (approximately 5 g) could be washed, filtered, and dried. All synthetic
237 minerals were dried then ground prior to analysis; see Table 1 for the synthetic Fe mineral
238 maximum and average grain and minimum crystallite sizes. The characterisation of all Fe
239 minerals, natural and synthetic, was performed by both XRD (Appendix A) and MBS
240 (Appendix B).

241 **2.2 XRD**

242 The mineralogy of the natural Ivigtut siderite and synthetic magnetite samples was analysed
243 using a PANalytical X'Pert PRO diffractometer at the National Museums Collection Centre
244 (Edinburgh, UK) using CuK α radiation, and identified by comparison with the International
245 Centre for Diffraction Data database, PDF-2, using X'pert High Score software. The
246 mineralogy of the synthetic 2-line ferrihydrite, synthetic goethite, and natural NMS and NAu-
247 2 nontronite samples was analysed likewise at Cardiff University with a monochromator to
248 reduce Fe fluorescence.

249 **2.3 Mineral grain size**

250 At least three photomicrographs were made of each ground Fe mineral under transmitted
251 light prior to analysis. Examples of these can be found in Fig. 2. The photomicrographs were
252 individually processed using Fiji (Schindelin et al., 2012). In Fiji, the images were
253 individually binarized and threshold adjusted (manually, using the sliding scale in the
254 threshold tool) to define every visible mineral grain. Grain clusters were erased from the
255 original photomicrograph where no clear border between separate mineral grains could be



256

257 *Figure 2: (1.5-column fitting image, in full colour online only) Photomicrographs of the Fe minerals used in this study*
 258 *under transmitted light. a) Ivigtut siderite (natural), b) 2-line ferrihydrite (synthetic), c) goethite (synthetic), d) UoE goethite*
 259 *(natural), e) magnetite (natural), f) NMS nontronite (natural), and g) NAu-2 nontronite.*

260 seen. All sizes (from 0 to infinity) and shapes (with circularity set from 0 – 1) of particles
 261 were analysed, exclusive of particles overlapping the edge of the photomicrograph, which
 262 were discarded. The maximum Feret particle dimensions are reported in Table 1. Grains less
 263 than 5 μm in diameter could not be reliably defined; these data were also discarded.

264 XRD data for each Fe mineral was combined with the Scherrer equation (Equation 1), as
 265 described in Guilbaud et al. (2010), on each identified 2θ peak, to roughly estimate the
 266 average crystallite (sub-micrometre particle) diameter of the smallest (and most reactive)
 267 particles that were excluded from the Fiji image analysis. The Scherrer equation defines the
 268 lower bound of crystallite size to the broadening of a specific 2θ peak in an XRD spectrum:

269

$$\text{Equation 1}$$

270

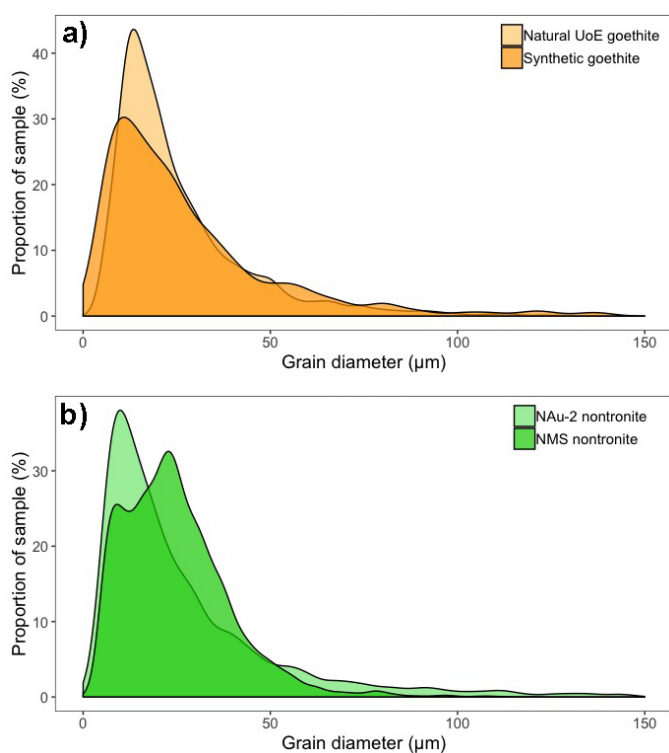
$$L = K\lambda(\beta\cos\theta)^{-1}$$

271 where L is crystallite diameter, the Scherrer constant (K) used is 0.91 assuming spherical
 272 particles (Brindley, 1980), λ is the wavelength of the X-ray (0.154 nm for $\text{CuK}\alpha$), β is the full
 273 width of the peak at half maximum (FWHM, in radian) and θ (in radian) is the angle of the
 274 peak.

		Ivigtut siderite (natural)	2-line ferrihydrite (synthetic)	goethite (synthetic)	UoE goethite (natural)	magnetite (synthetic)	NMS nontronite (natural)	NAu-2 nontronite (natural)
Particle diameter (μm)	Maximum	177 \pm 18	236 \pm 12	161 \pm 16	172 \pm 17	157 \pm 16	119 \pm 12	208 \pm 21
	Average	16 \pm 2	19 \pm 1	28 \pm 3	26 \pm 3	25 \pm 3	25 \pm 3	28 \pm 3
	n_p	3425	885	835	4024	3346	4484	3780
Crystallite diameter (nm)	Minimum	53	0.6	14	15	12	3	2
	Average	57	0.8	21	25	17	9	6
	n_c	2	2	4	4	4	4	5

275 *Table 1: Maximum and average Feret diameter (μm), and number of sampled grains (n_p) used to measure Fe mineral grain size. All mineral grain size analyses were performed using the Fiji*
276 *Image J software. Minimum and average crystallite diameters (nm), and number of 2 θ peaks (n_c) used to estimate crystallite size. All crystallite diameters were estimated from the Scherrer*
277 *equation (Equation 1); a precision of ± 9 nm was determined from 5 repeat measurements of the same sample.*

278 Table 1 reports the average and maximum grain size values calculated using Fiji, and the
 279 estimated minimum and average crystallite diameters using the XRD data combined with the
 280 Scherrer equation (Equation 1). The reported errors for the Fiji-analysed grain sizes represent
 281 the minimum size at which particles could be identified for the specific magnification: for
 282 photomicrographs magnified by 2X – 4X and 10X – 20X, this is $\pm 10\%$ and $\pm 5\%$
 283 respectively. The precision on L was ± 9 nm, as calculated from 5 repeat measurements of the
 284 UoE goethite sample. Grain size distribution is also compared between the two goethite and
 285 between the two nontronite samples used in this study, in Fig. 3.



286

287 *Figure 3: (single-column fitting image, in full colour online only) Distribution of mineral grain size throughout unleached,*
 288 *ground, and homogenised mineral samples. a) natural UoE and synthetic goethite, and b) NMS nontronite and NAu-2*
 289 *nontronite. Mineral grain size analyses were performed using the Fiji Image J software.*

290

291 2.4 Sequential Fe extraction

292 A mixed Fe mineral standard (CARB-2: approximately 30 % siderite, 20 % ferrihydrite, 20
 293 % goethite, 15 % magnetite, and 15 % nontronite) was made to represent an example of the
 294 Fe mineral assemblage (not the entire mineral assemblage) that may occur in natural marine

295 sediments, using just one mineral from each target Fe mineral phase in the extraction
296 sequence. Each of the selected Fe minerals and the mixed Fe mineral standards were run
297 through the full sequential extraction protocol shown in Fig. 1. Each stage of the same
298 protocol was also performed non-sequentially on the individual Fe mineral targeted by that
299 particular stage: whereby only Fe_{aca-48} was run for siderite; only Fe_{hyam} was run for 2-line
300 ferrihydrite; only Fe_{di-ct} was run for goethite; and Fe_{oxa} was run for magnetite. The $Fe_{HCl-1min}$
301 stage is not designed to specifically target nontronite. $Fe_{HCl-1min}$ was therefore run
302 individually for nontronite to test the effectiveness of nontronite dissolution by a 1-minute
303 boil in HCl (as described below). Each non-sequential, single mineral extraction was
304 performed in triplicate; the average value from each extraction is presented in Table 2.

305 Total Fe was extracted from approximately 0.1 g of the ground, dried, and unleached
306 individual and mixed Fe mineral samples using a three-stage digestion procedure: 4 ml aqua
307 regia; 2 ml HF; 2 ml HNO_3 . The digestions were each performed in Teflon beakers left on a
308 hotplate at 90 °C for 24 hours, dried completely, and cooled before adding the next reagent.
309 All samples were finally redissolved in 2 % HNO_3 for dilution and Fe concentration analysis
310 by atomic absorption spectrometry (AAS).

311 The modified Poulton and Canfield (2005) Fe extraction scheme was run as described in Fig.
312 1. All citrate-buffered dithionite solutions were prepared using fresh dithionite powder
313 immediately before each batch of Fe_{di-ct} extractions. The ‘ Fe_{aca-48} ’ and ‘ $Fe_{HCl-1min}$ ’
314 terminology denotes variations to the standard ‘ Fe_{aca} ’ and ‘ Fe_{HCl} ’ Poulton and Canfield
315 (2005) methods, which we employed during the first and last stages of our sequential
316 protocol (Fig. 1). We used the longer (48, rather than 24 hours) and hotter (50 °C, rather than
317 room temperature) Na-acetate leach to target our highly-crystalline Ivigtut siderite sample, as
318 recommended in Poulton and Canfield (2005). However, this more aggressive leach is rarely
319 used in sequence on modern sediments since it is likely to cause premature leaching of

320 subsequent Fe minerals, such as ferrihydrite, as is observed in this study. The Fe_{aca-48}
321 extraction is more readily applied to ancient sediments, in which ferrihydrite is rarely found
322 (Cornell and Schwertmann, 2003), and premature removal of this easily-reducible Fe oxide is
323 not an issue. All extraction stages were performed in sealed centrifuge tubes on a shaker table
324 under oxic conditions, except $Fe_{HCl-1min}$. In the final $Fe_{HCl-1min}$ extraction, 12 N HCl was
325 heated on a hotplate in a glass beaker and, once boiling, the sample was added and stirred
326 into the reagent. After boiling for exactly 1 minute, the solution was quenched immediately
327 with ultra-pure H_2O (18.2 M Ω .cm), then decanted for centrifugation. At the end of each
328 extraction stage (Fig. 1) the suspension was centrifuged at 6000 rpm for 10 minutes, which
329 allowed the leachate to be carefully pipetted from the residual solid sample. The leachate was
330 subsampled and diluted in 2 % HNO_3 ready for Fe analysis by AAS. 0.05 – 0.15 g of washed
331 (three times with ultra-pure H_2O (18.2 M Ω .cm) and re-centrifuged) and dried (at 30 °C
332 overnight) sample was removed for analysis by MBS.

333 A sample mass : reagent volume ratio (S:R) of <2.5 (Thompson et al., 2019) was applied to
334 each stage of the extraction to avoid saturation of the reagent by the sample. The S:Rs used to
335 extract the Fe mineral phases in this study were much lower than that recommended by
336 Poulton and Canfield (2005) for natural sediment: 0.1 – 0.2 g : 10 ml. Since our experiment
337 required the removal of 40 – 60 mg after each stage for MBS analysis, all extractions were
338 performed in triplicate to ensure sufficient residual material was available for each
339 subsequent MBS subsampling, while maintaining an optimal S:R ratio. Following each
340 extraction, the material was combined and homogenised for MBS analysis, then divided back
341 into triplicate to maintain a suitably-low S:R. As residual material was removed for MBS
342 analysis, the S:R was gradually reduced throughout the sequence: ~2.5 in Fe_{aca-48} , ~2.1 in
343 Fe_{hyam} , ~1.7 in Fe_{di-ct} , ~1.3 in Fe_{oxa} , and ~0.8 in $Fe_{HCl-1min}$. Thompson et al. (2019)
344 recommend a lower S:R of ~0.75 for Fe_{di-ct} , than was used herein; the possible implications

345 of this are discussed in Section 3.1. No residue was left for MBS analysis following the
346 stages that completely extracted the target mineral. The total digestions were run separately,
347 rather than as the final stage in the extraction sequence. The entire procedure (Fig. 1) was
348 repeated 3 times for each individual mineral and the mixed Fe mineral standard (each
349 performed in triplicate) to initially produce a total of 9 leachate results, and three batches of
350 residual material per sample; the number of samples (n) from each extraction stage
351 continually reduced throughout the sequence as more material was removed for MBS. The
352 average values and n from each extraction stage run in sequence for the individual Fe
353 minerals and the mixed Fe mineral standards (CARB-2 and CARB-3) are respectively
354 presented in Tables 3 and 4.

355 **2.5 Atomic Absorption Spectroscopy (AAS)**

356 The Fe concentration in the final leachate and digest solutions was determined on a Unicam
357 989 AA Spectrometer at the University of Stirling (UK) and calibrated using matrix-matched
358 single element Fe standards. The diluted solutions were run in a random sequence and all
359 measurements were blank and drift corrected. Measured concentrations of the certified
360 reference material (CRM) SdAR-H1 (blended metalliferous sediment) were accurate to $\pm 5\%$
361 of the value reported by the International Association of Geoanalysts ([http://iageo.com/wp-](http://iageo.com/wp-content/uploads/2017/11/SdAR-H1_RM_data_sheet-1.pdf)
362 [content/uploads/2017/11/SdAR-H1_RM_data_sheet-1.pdf](http://iageo.com/wp-content/uploads/2017/11/SdAR-H1_RM_data_sheet-1.pdf)). Analytical precision was < 6
363 %RSD, from replicate analysis of randomly chosen samples and the SdAR-H1 CRM. The Fe
364 concentrations extracted by single stage individual mineral extractions only, the full sequence
365 (see Fig. 1) of individual mineral extractions, and mixed Fe mineral sequential extractions is
366 respectively reported in Tables 2, 3 and 4.

367 **2.6 Mössbauer Spectroscopy (MBS)**

368 The presence, absence, and relative proportion of specific Fe mineral phases in leached
369 sample residues was confirmed by room temperature ^{57}Fe MBS (Gütlich and Schröder,

2012), using a standard transmission Mössbauer spectrometer (Wissel, Germany) with a ^{57}Co in Rh matrix radiation source in constant acceleration mode, at the University of Stirling (UK). 0.05 – 0.15 g of dried, homogenised sample was loaded into sealed acrylic discs with a circular cross section of approximately 1 cm². Troughs in transmission spectra represent absorption maxima; the area beneath each subspectrum represents the relative contribution of the specific Fe mineral phase to the observed/fitted MBS absorption spectrum (Figs. 4 – 5). The MBS spectra were analysed using the Voigt-based fitting routine (Rancourt and Ping, 1991) as implemented in the Recoil software (University of Ottawa, Canada). Following the Voigt-based fitting, we compared hyperfine parameters (including isomer shift (δ) in mm s⁻¹, quadrupole splitting (ΔEQ) in mm s⁻¹, and internal magnetic field (B_{hf}) in T) of each subspectrum with those of library reference spectra. All MBS data can be found in tables C1 – C4 of the Appendix.

3. RESULTS

3.1 Single and sequential extraction of individual Fe mineral samples

Fe_{hyam} and Fe_{oxa} were the only stages to fully extract the target Fe mineral phase from the pure mineral samples. The extraction behaviour of the single Fe minerals differed between different natural samples, and between natural and synthetic variants of the same mineral.

The igneous Ivigtut siderite was particularly resistant to extraction by sodium acetate (Table 2). Less than 15 % of the total siderite Fe was collected by the individual $\text{Fe}_{\text{aca-48}}$ stage (Table 2), even when a 48-hour leach at pH 4.5 and 50 °C was applied, as recommended by Poulton and Canfield (2005) for crystalline siderite samples. MBS also identified siderite in the residual material of each extraction stage up to and including Fe_{oxa} (Table 3) before it was fully removed in $\text{Fe}_{\text{HCl-1min}}$; although 23 – 44 % of the siderite was dissolved as Fe_{hyam} (Table 3).

Sample	Target extraction	Total Fe available for extraction	Fe extracted in target stage	Post-extraction MBS
Iviglut siderite (natural)	Fe _{aca-48}	46.9 ± 2.1 (n = 3)	3.9 ± 0.2 (n = 3)	P
2-line ferrihydrite (synthetic)	Fe _{hyam}	47.2 ± 2.1 (n = 3)	41.6 ± 1.8 (n = 2)	A
goethite (synthetic)	Fe _{di-ct}	63.2 ± 2.8 (n = 3)	60.1 ± 2.6 (n = 3)	A
UoE goethite (natural)	Fe _{di-ct}	56.6 ± 2.5 (n = 3)	23.8 ± 1.0 (n = 3)	P
magnetite (synthetic)	Fe _{oxa}	72.2 ± 3.2 (n = 3)	75.5 ± 3.3 (n = 3)	A
NMS nontronite (natural)	Fe _{HCl-1min}	24.5 ± 1.1 (n = 3)	12.5 ± 0.5 (n = 3)	P
NAu-2 nontronite (natural)	Fe _{HCl-1min}	19.3 ± 0.8 (n = 3)	1.8 ± 0.1 (n = 3)	P

396

397

398

399

400

Table 2: Average Fe contents (wt.%) for each individual extraction stage compared with the average total Fe (wt.%) dissolved in the bulk HF / HNO₃ digest. Each extraction stage was performed non-sequentially using the single target Fe mineral for each stage: only siderite was run through Fe_{aca-48}; only 2-line ferrihydrite was run through Fe_{hyam}; only goethite was run through Fe_{di-ct}; only magnetite was run through Fe_{oxa}; and only nontronite was run through Fe_{HCl-1min}. MBS analyses were conducted on residual material left from the target extractions; the presence (P) or absence (A) of each individual mineral in the post-extraction residue is shown in the final column. 'n' = number of samples.

Sample	Target extraction	Total Fe available for extraction	Fe extracted in Fe _{aca-48}	Post-Fe _{aca-48} MBS	Fe extracted in Fe _{hyam}	Post- Fe _{hyam} MBS	Fe extracted in Fe _{di-ct}	Post-Fe _{di-ct} MBS
Ivigtut siderite (natural)	Fe _{aca-48}	46.9 ± 2.1 (n = 3)	1.5 ± 0.1 (n = 9)	P +	15.3 ± 0.7 (n = 8)	P +	2.6 ± 0.1 (n = 6)	P -
2-line ferrihydrite (synthetic)	Fe _{hyam}	47.2 ± 2.1 (n = 3)	6.8 ± 0.3 (n = 7)	P	44.2 ± 1.9 (n = 6)	A	ND	A
goethite (synthetic)	Fe _{di-ct}	63.2 ± 2.8 (n = 3)	BDL (n = 9)	P	± 0.0 (n = 9)	P -	54.6 ± 2.4 (n = 7)	A
UoE goethite(natural)	Fe _{di-ct}	56.6 ± 2.5 (n = 3)	0.0 ± 0.0 (n = 9)	P	0.1 ± 0.0 (n = 8)	P	35.8 ± 1.6 (n = 4)	P
magnetite (synthetic)	Fe _{oxa}	72.2 ± 3.2 (n = 3)	0.0 ± 0.0 (n = 9)	P	0.6 ± 0.0 (n = 8)	P	31.4 ± 1.4 (n = 5)	P
NMS nontronite (natural)	Fe _{HCl-1min}	24.5 ± 1.1 (n = 3)	± 0.0 (n = 9)	P -	0.9 ± 0.0 (n = 6)	P -	13.8 ± 0.6 (n = 4)	P
NAu-2 nontronite (natural)	Fe _{HCl-1min}	19.3 ± 0.8 (n = 3)	± 0.0 (n = 9)	P	1.0 ± 0.0 (n = 6)	P	9.6 ± 0.4 (n = 6)	P

402

403

404

405

406

407

408

409

410

Table 3 Average Fe contents (wt.%) of sequential mineral leachates, compared with the average total Fe (wt.%) dissolved in the bulk HF/HNO₃ digest. All extraction stages (Fig. 1) were run sequentially on each individual Fe mineral. Fe_{HCl-24} (redefined from “unreactive silicate” or “Fe_{US}”, (Poulton and Canfield, 2005)) refers to the unreactive Fe pool that remains unextracted after the sample is ashed at 450 °C for 8 hours and near-boiled in 6 N HCl for 24 hours. The average values shown in Tables 2 – 4 represent data ranges that are often highly variable, due to the operational nature and consequent unreliable reproducibility of sequential extraction protocols. MBS analyses were conducted on residual material left from the target extractions; the presence (P) or absence (A) of each individual mineral in the post-extraction residue is shown in the final column; ‘+’ and ‘-’ indicate a noticeable increase and decrease, respectively, in the relative amount of a mineral compared with the previous extraction stage. ‘P’ without ‘+’ or ‘-’ indicates no noticeable change. The cumulative total Fe adds together all of the sequentially-extracted Fe, for comparison with the total Fe initially available for extraction in the unleached Fe mineral phases (errors calculated by adding the individual errors in quadrature). BDL = below detection limit, ND = no data.

411

Sample	Target extraction	Total Fe available for extraction	Fe extracted in Fe _{oxa}	Post-Fe _{oxa} MBS	Fe extracted in Fe _{HCl-1min}	Post- Fe _{HCl-1min} MBS	Fe extracted in Fe _{HCl-24}	Post-Fe _{HCl-24} MBS	Cumulative total Fe
Ivigtut siderite (natural)	Fe _{aca-48}	46.9 ± 2.1 (n = 3)	2.4 ± 0.1 (n = 2)	P +	32.7 ± 1.4 (n = 2)	A	ND	A	54.5 ± 1.6
2-line ferrihydrite (synthetic)	Fe _{hyam}	47.2 ± 2.1 (n = 3)	ND	A	ND	A	ND	A	51 ± 1.9
goethite (synthetic)	Fe _{di-ct}	63.2 ± 2.8 (n = 3)	ND	A	ND	A	ND	A	54.6 ± 2.4
UoE goethite (natural)	Fe _{di-ct}	56.6 ± 2.5 (n = 3)	0.6 ± 0.0 (n = 2)	P	27.0 ± 1.6 (n = 2)	P -	ND	A	63.5 ± 2.3
magnetite (synthetic)	Fe _{oxa}	72.2 ± 3.2 (n = 3)	44.8 ± 2.0 (n = 1)	A	ND	A	ND	A	76.8 ± 2.6
NMS nontronite (natural)	Fe _{HCl-1min}	24.5 ± 1.1 (n = 3)	1.5 ± 0.1 (n = 3)	P	1.6 ± 0.0 (n = 1)	P	0.9 ± 0.0 (n = 1)	A	18.8 ± 1.9
NAu-2 nontronite (natural)	Fe _{HCl-1min}	19.3 ± 0.8 (n = 3)	0.7 ± 0.0 (n = 4)	P -	2.9 ± 0.1 (n = 3)	P -	5.1 ± 0.2 (n = 1)	A	19.3 ± 3.1

412

413 *Table 3 continued.*

	Extraction stage	Total Fe available for extraction	Fe extracted in target stage	Post-extraction MBS				
				Ivigtut siderite	2-line ferrihydrite	goethite	magnetite	nontronite
CARB-2	Fe _{UL}	49.0 ± 2.1 (n = 3)		P	P	P	P	P
	Fe _{aca-48}	15.1 ± 0.6	14.8 ± 0.6 (n = 9)	<u>P</u> -	P -	P	P	P - (S)
	Fe _{hyam}	10.7 ± 0.4	3.9 ± 0.4 (n = 8)	P	<u>A</u>	P +	P +	P + (S)
	Fe _{di-ct}	10.6 ± 0.4	25.5 ± 1.1 (n = 6)	P +	A	<u>P</u> -	P	P (S)
	Fe _{oxa}	6.3 ± 0.3	24.0 ± 1.1 (n = 4)	P	A	P	<u>A</u>	A
	Fe _{HCl-1min}	6.3 ± 0.3	38.4 ± 1.7 (n = 1)	A	A	A	A	<u>A</u>
CARB-3	Fe _{UL}	46.8 ± 2.1 (n = 3)		P	P	P	P	P
	Fe _{aca-48}	14.5 ± 0.6	14.9 ± 0.7 (n = 9)	<u>P</u>	P -	P	P	P -
	Fe _{hyam}	9.8 ± 0.4	3.9 ± 0.2 (n = 7)	P	<u>A</u>	P	P	P
	Fe _{di-ct}	10.3 ± 0.4	30.0 ± 1.3 (n = 6)	P +	A	<u>P</u> -	P -	P +
	Fe _{oxa}	6.1 ± 0.3	18.8 ± 0.8 (n = 5)	P	A	P -	<u>A</u>	P
	Fe _{HCl-1min}	6.1 ± 0.3	31.5 ± 1.4 (n = 3)	P -	A	A	A	<u>P + (S)</u>
	Fe _{HCl-24}		4.9 ± 0.2 (n = 1)	A	A	A	A	A

414 Table 4: Average Fe contents (wt.%) of sequential mixed mineral leachates, compared with the average total Fe (wt.%) dissolved in the bulk HF/HNO₃ digest. The total Fe available for each
415 extraction stage was calculated by dividing the total Fe_{UL} content by the known proportion of each mineral mixed into the CARB-2 and CARB-3 samples. All extraction stages (Fig. 1) were run
416 sequentially on the CARB-2 and CARB-3 Fe mineral mixtures. Fe_{HCl-24} (redefined from “unreactive silicate” or “Fe_{US}”, (Poulton and Canfield, 2005)) refers to the unreactive Fe pool that
417 remains unextracted after the sample is ashed at 450 °C for 8 hours and near-boiled in 6 N HCl for 24 hours. No ‘unreactive silicate’ Fe minerals, as defined by Poulton and Canfield (2005),

418 were used in this study (hence there is no Fe available for the Fe_{HCl-24} extraction stage), however the Fe_{HCl-24} stage was required to dissolve the residual nontronite following Fe_{HCl-1min}. The
419 average values reported here often represent a wide data range (low minimum and high maximum values) that exemplify the effects of non-target mineral extraction as discussed in the text.
420 MBS analyses were conducted on residual material left from the target extractions. The presence (P) or absence (A) of each individual mineral in the post-extraction residue is reported
421 alongside any noticeable changes in the shape of an Fe mineral peak and a consequent modification of the mineral-specific parameters (S); '+' and '-' indicate a noticeable increase and
422 decrease, respectively, in the relative mineral proportion compared with the previous extraction stage. 'P' without '+' or '-' indicates no noticeable change. The target mineral (underlined) of
423 each extraction stage is highlighted in bold where the target extraction is successful, and italicised where incomplete. BDL = below detection limit, ND = no data.

424 Synthetic 2-line ferrihydrite was completely removed during its target (Fe_{hyam}) stage (Table 2
425 and Table 3). However, 15 % of the ferrihydrite Fe was leached in $\text{Fe}_{\text{aca-48}}$ (Table 3), likely
426 due to the use of the extended Na-acetate leach in sequence (as discussed in Section 4.1).

427 More than 90 % of the total Fe available in the synthetic goethite was removed by $\text{Fe}_{\text{di-ct}}$
428 when this stage was run individually (Table 2), and more than 80 % was removed when $\text{Fe}_{\text{di-ct}}$
429 was run sequentially (Table 3). According to the Mössbauer spectra that accompany the
430 sequential extraction of synthetic goethite, the abundance of synthetic goethite Fe was not
431 affected by $\text{Fe}_{\text{aca-48}}$ and was slightly lowered for Fe_{hyam} . Synthetic goethite was removed
432 completely by $\text{Fe}_{\text{di-ct}}$ – the target stage (Table 3). There was insufficient residual material for
433 MBS analysis, following both the individual and sequential extraction of synthetic goethite
434 (Tables 2 and 3, respectively). $\text{Fe}_{\text{di-ct}}$ was therefore considered effective when synthetic
435 goethite was the only mineral present.

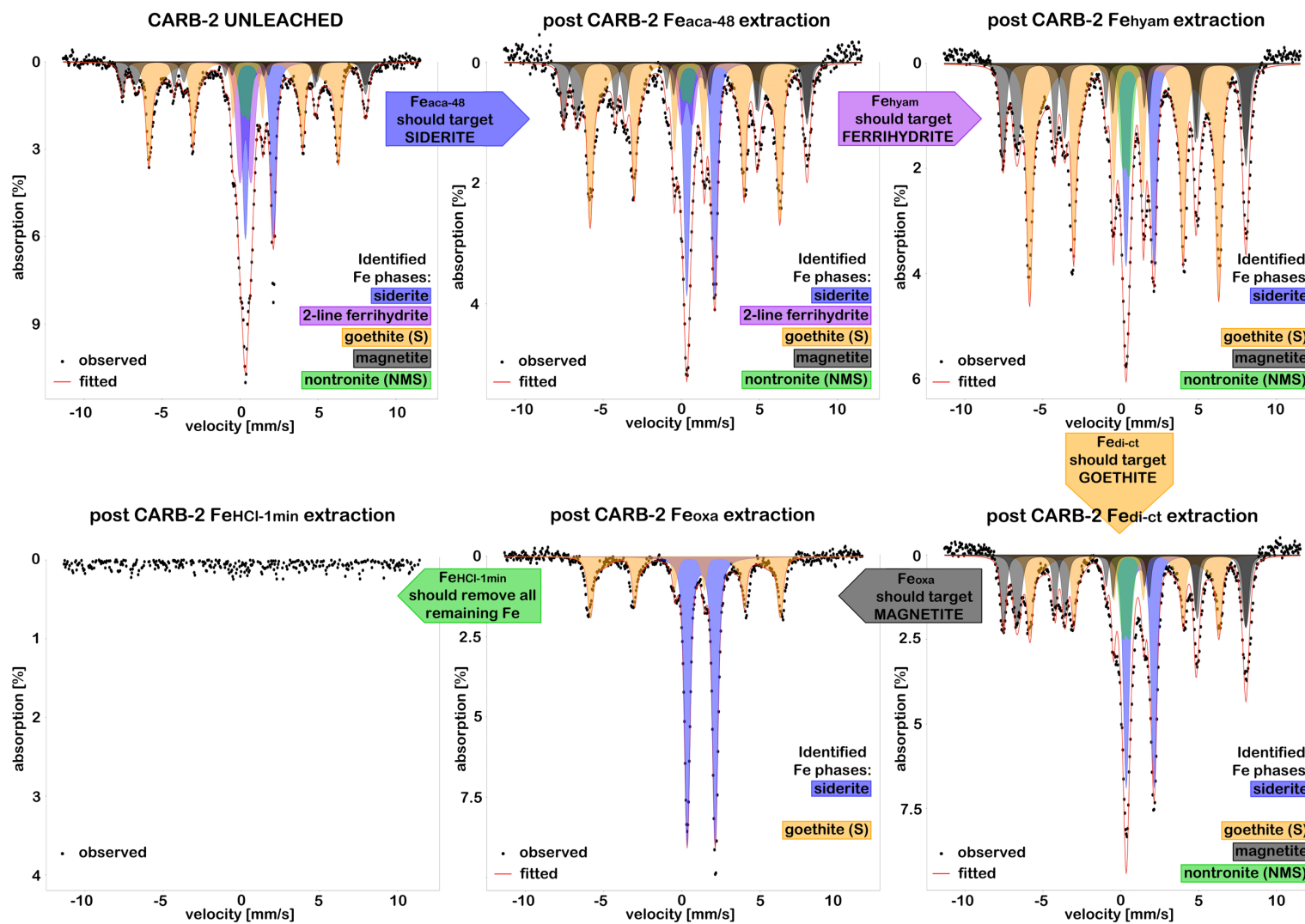
436 Natural UoE goethite was more resistant to the target extraction than its synthetic form
437 (Table 2). Only 36 – 47 % of the total Fe in the UoE goethite was recovered during the
438 individual $\text{Fe}_{\text{di-ct}}$ stage and the UoE goethite remained clearly visible in the residual material
439 MB spectrum (Table 2). Up to 82 % of the total Fe was, however, recovered by the sequential
440 $\text{Fe}_{\text{di-ct}}$ stage of the natural UoE goethite extraction (Table 3); all remaining UoE goethite Fe
441 was recovered during $\text{Fe}_{\text{HCl-1min}}$. MBS identified UoE goethite in the residual material of each
442 sequential extraction stage, including $\text{Fe}_{\text{HCl-1min}}$ (Table 3), although the abundance of natural
443 goethite was noticeably reduced by $\text{Fe}_{\text{HCl-1min}}$.

444 AAS leachate and MBS residue results suggest that both the individual (Table 2) and
445 sequential (Table 3) Fe_{oxa} extractions effectively targeted all of the synthetic magnetite Fe,
446 although up to 66 % was solubilised during the previous, sequential $\text{Fe}_{\text{di-ct}}$ stage (Table 3).

447 Mössbauer spectra of the individual (Table 2) and sequential (Table 3) $\text{Fe}_{\text{HCl-1min}}$ extractions
448 show that successive stages of the extraction procedure dissolved an increasing amount of
449 both natural nontronite samples, with the final $\text{Fe}_{\text{HCl-1min}}$ stage solubilising the majority of the
450 available nontronite Fe. The $\text{Fe}_{\text{HCl-1min}}$ extraction is not specific to nontronite but should
451 dissolve the remaining Fe that is poorly reactive towards sulphide (Raiswell and Canfield,
452 1996). The individual $\text{Fe}_{\text{HCl-1min}}$ stage yielded 48 – 55 % of the available NMS Fe and just 9
453 % of the available N Au-2 Fe (Table 2). 47 – 67 % of the NMS nontronite Fe and 47 – 53 %
454 of the N Au-2 nontronite Fe was removed by the sequential $\text{Fe}_{\text{di-ct}}$ stage (Table 3). Nontronite
455 removal during $\text{Fe}_{\text{di-ct}}$ was likely responsible for the low Fe yield recovered from the residual
456 NMS (< 6 %) and N Au-2 (< 17 %) nontronite samples during the sequential $\text{Fe}_{\text{HCl-1min}}$ stage
457 (Table 3).

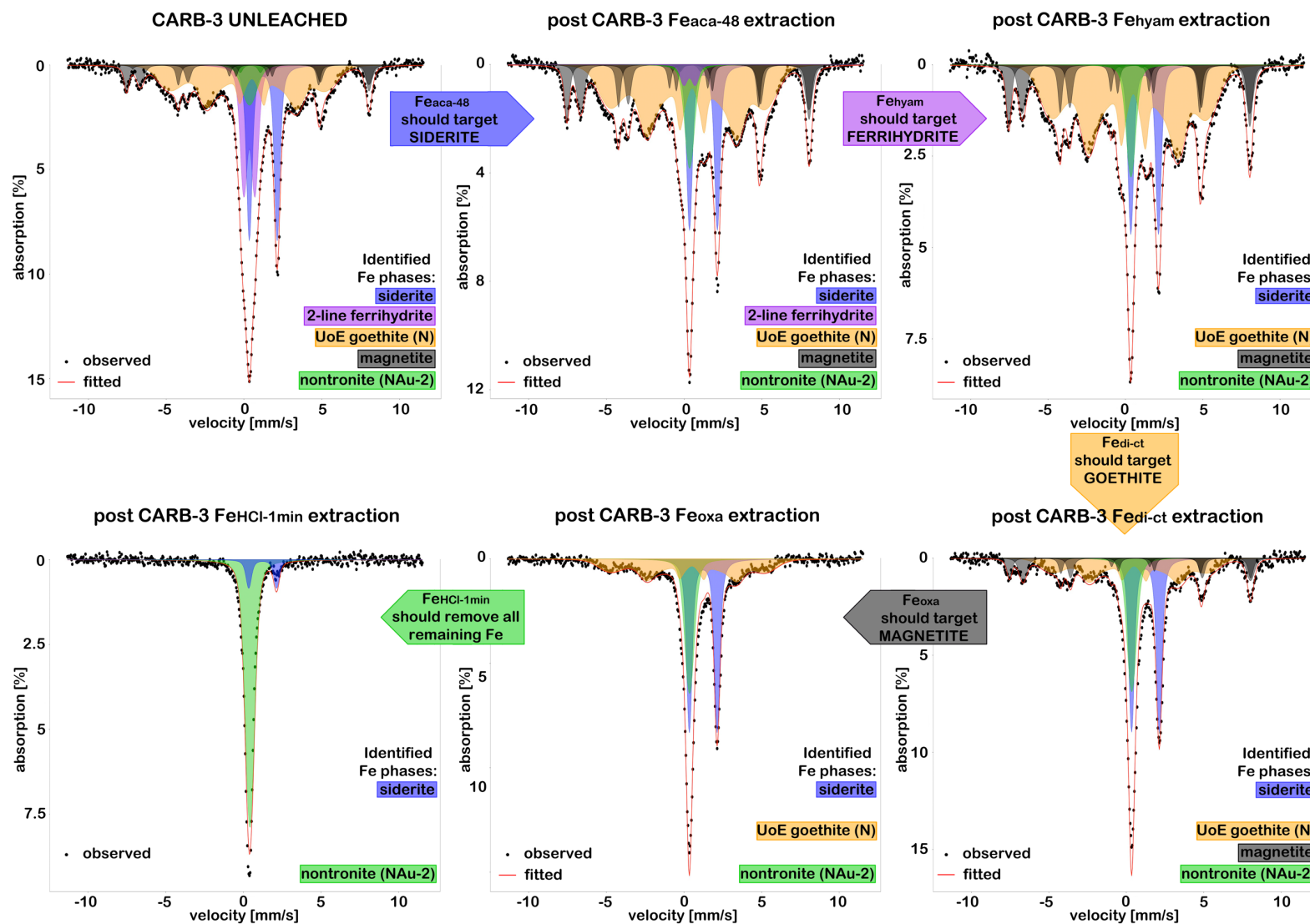
458 **3.2 Sequential extraction of mixed Fe mineral samples**

459 The efficiency with which individual extraction stages dissolved their target minerals was
460 further complicated by the presence of other minerals. Every stage, excluding the final $\text{Fe}_{\text{HCl-1min}}$,
461 exhibited the removal of non-target Fe minerals that should not have been affected until
462 later on in the leach sequence. Fe_{hyam} and Fe_{oxa} were, again, the only stages to completely
463 remove their target minerals when present in an Fe mineral mixture. Following the observed
464 incomplete extraction of natural goethite Fe, compared with the successful removal of
465 synthetic goethite and the extraction of natural NMS nontronite Fe during the individual $\text{Fe}_{\text{di-ct}}$
466 stage (Tables 2 and 3), another mixed Fe mineral standard, CARB-3, was created to further
467 test yield efficiency. CARB-3 included Ivigtut siderite, synthetic 2-line ferrihydrite, and
468 synthetic magnetite in the same proportions as CARB-2, but the 20 % synthetic goethite and
469 15 % natural NMS nontronite were respectively replaced with 20 % natural UoE goethite and
470 15 % natural N Au-2 nontronite.



471

472 *Figure 4: (2-column fitting image, in full colour online and print) Comparison of MBS spectra from the unleached and leached CARB-2 mixed mineral standard after each stage in the full*
 473 *sequential extraction. No Fe was present following the final Fe_{HCl-1min} stage.*



474

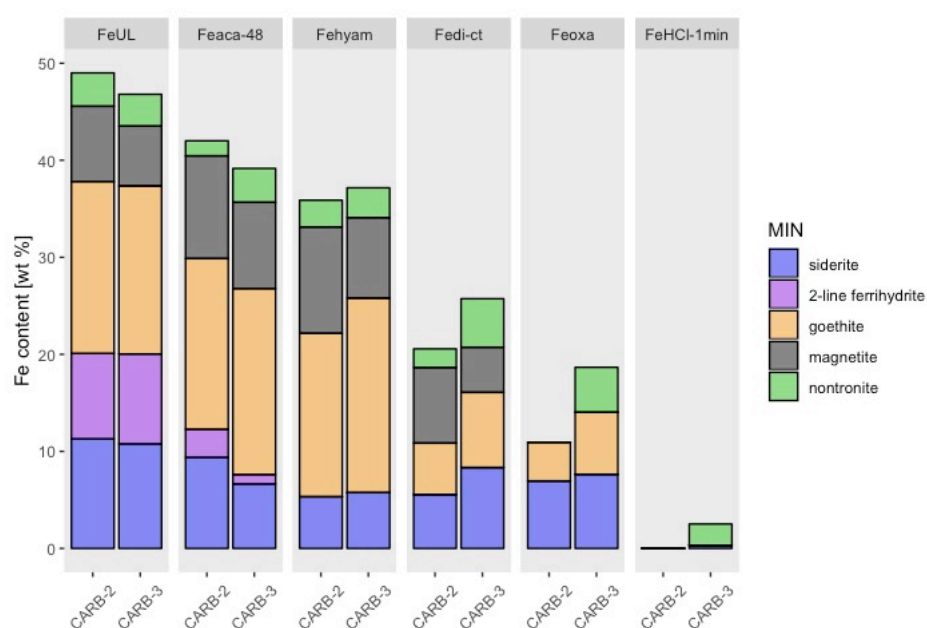
475 *Figure 5: (2-column fitting image, in full colour online and print) Comparison of MBS spectra from the unleached and leached CARB-3 mixed mineral standard after each stage in the full*
 476 *sequential extraction.*

477 The unleached CARB-2 and CARB-3 samples respectively contained 26 % and 27 % Ivigtut
478 siderite. 26 – 35 % of the total Fe available in the unleached CARB-2 and CARB-3 samples
479 was removed during the Fe_{aca-48} stage (Table 4), which implies that all siderite Fe was
480 successfully removed by its target extraction. MBS analysis of the accompanying Fe_{aca-48}
481 residue, clearly identified the presence of siderite in both CARB-2 (Fig. 4) and CARB-3 (Fig.
482 5) samples after the target extraction stage. In fact, siderite continued to dominate sample
483 composition until it was completely removed during Fe_{HCl-24} (a stage that is usually only
484 required for unreactive silicate extraction). Although siderite should be the only mineral
485 targeted by Na acetate, the relative proportion of 2-line ferrihydrite and NMS nontronite
486 (included in CARB-2) was noticeably reduced (Fig. 4). NAu-2 nontronite (included in
487 CARB-3) was unaffected by Fe_{aca-48} (Fig. 5).

488 Synthetic 2-line ferrihydrite comprised 24 % of the unleached CARB-2 sample and 14 % of
489 the unleached CARB-3 sample. Fe_{hyam} removed 15 – 20 % of the total Fe available in CARB-
490 2, and 8 – 9 % of the total Fe available in CARB-3 (Table 4). MBS confirmed the complete
491 removal of all remaining 2-line ferrihydrite Fe during the target Fe_{hyam} stage (and the removal
492 of some 2-line ferrihydrite during Fe_{aca-48}) in both CARB-2 (Fig. 4) and CARB-3 (Fig. 5).

493 Synthetic goethite accounted for 28 % of the unleached CARB-2 sample, while 34 % of
494 CARB-3 consisted of natural UoE goethite. The CARB-2 Fe_{di-ct} leachate contained a highly
495 variable 23 – 71 % of the total available Fe (Table 4), which suggests incomplete synthetic
496 goethite dissolution at the lower bound, and dissolution of both synthetic goethite and other
497 mineral phases at the higher bound. The average dithionite-associated Fe content in the Fe_{di-ct}
498 CARB-2 residue was noticeably reduced in comparison to that of the previous Fe_{hyam} stage
499 (Fig. 4), but synthetic goethite was clearly identified in the residual material of the target Fe_{di-}
500 ct and the following Fe_{oxa} stages (Fig. 4), which supports the incomplete dissolution of the
501 target mineral during Fe_{di-ct} . The CARB-3 Fe_{di-ct} leachate conversely contained 43 – 52 % of

502 the total Fe available in the unleached CARB-3 sample (Table 4), up to 18 % more Fe than
 503 was actually available from the natural UoE goethite component. From the individual mineral
 504 extraction results (Table 3) and modified parameters in the CARB-3 Fe_{hyam} and Fe_{di-ct} MBS
 505 spectra (Table A1), it is likely that the overestimated Fe_{di-ct} yield (in both CARB-2 and
 506 CARB-3) came from the dissolution of magnetite Fe and NAu-2 nontronite Fe in sodium
 507 dithionite. Following the removal of the majority of the UoE goethite during Fe_{di-ct} , siderite
 508 and nontronite dominated the residual CARB-3 material (Fig. 5).



509
 510 *Figure 6: (1.5-column fitting image, in full colour online and print) Fe content in CARB-2 and CARB-3 throughout the*
 511 *extraction sequence. This figure shows a semi-quantitative estimation of the average Fe content (wt %) extracted from all*
 512 *minerals at each stage of the sequential leach for the mixed Fe mineral samples, CARB-2 and CARB-3. Results combined*
 513 *the known quantity of Fe released in the leachate at each extraction stage (measured by AAS) and the known proportion of*
 514 *minerals identified (by MBS) in the residual material.*

515 All magnetite Fe present in the unleached CARB-2 and CARB-3 samples (13 – 14 %) was
 516 extracted during Fe_{oxa} (Table 4), and no magnetite was detected by MBS in the residual
 517 CARB-2 (Fig. 4) or CARB-3 (Fig. 5) material following the target extraction. Magnetite Fe
 518 was therefore effectively targeted by Fe_{oxa} , but the Fe_{oxa} leachate Fe content far exceeded that
 519 provided by the dissolution of magnetite Fe alone: up to over 60 % in both CARB-2 and
 520 CARB-3 (Table 4). The simultaneous removal of NMS nontronite Fe in CARB-2 (Fig. 4),

521 and natural UoE goethite Fe in CARB-3 (Fig. 5), during Fe_{oxa} , explains the presence of
522 excess Fe in these samples. Residual siderite and synthetic goethite (from the target Fe_{aca-48}
523 and Fe_{di-ct} stages, respectively) appeared unaffected by Fe_{oxa} in CARB-2 and remained in the
524 residual material following the ammonium oxalate dissolution (Fig. 4); the same was true of
525 siderite and NAu-2 nontronite in CARB-3 (Fig. 5).

526 All Fe minerals were removed from CARB-2 by $Fe_{HCl-1min}$ (Fig. 4) and the residual material
527 was bleached white (identified via XRD as quartz that was originally present in the UoE
528 goethite and both nontronite samples). Almost all of the siderite was finally removed from
529 CARB-3 during $Fe_{HCl-1min}$, although a small signal still remained in the Mössbauer spectrum
530 (Fig. 5). The lingering Fe mineral signature post $Fe_{HCl-1min}$ in CARB-3 (Fig. 5) was that of the
531 NAu-2 nontronite, which appears more persistent than the NMS nontronite (possibly due to a
532 modification of the original Fe_{HCl} Berner (1970) method). The NAu-2 nontronite was
533 completely removed from CARB-3 by the final 24-hour boiling HCl stage, which was
534 designed to leach the unreactive sheet silicates (Poulton and Canfield, 2005).

535 **3.3 Mineral grain size and distribution**

536 Maximum and average particle diameters, and minimum and average crystallite diameters for
537 all the Fe minerals used in this study are shown in Table 1. Ivigtut siderite was the most
538 crystalline of the Fe minerals used herein (Fig. 1) with the smallest average grain size.
539 However, the most reactive components of a sample are the crystallite grains, due to their
540 larger surface area in comparison to the larger-diameter particles. Therefore, it is unsurprising
541 that siderite proved particularly resistant to dissolution, since the minimum size of the siderite
542 crystallites was more than twice that of all the other Fe minerals in this study. The natural
543 UoE goethite had a larger maximum diameter but a smaller average diameter than the
544 synthetic goethite and was more efficiently dissolved during its target Fe_{di-ct} stage (Table 2).
545 NMS nontronite had both a smaller maximum and a smaller average grain size than the NAu-

546 2 nontronite and was much more efficiently dissolved during its target $\text{Fe}_{\text{HCl-1min}}$ stage (Table
547 2). There was little difference in crystallite particle diameter between the two nontronite
548 samples.

549

550

4. DISCUSSION

551 4.1 Sequential extraction limitations

552 Meaningful comparison between sequential extraction experiments in different (and even
553 within the same) laboratories, is extremely difficult, due to i) the use and modification of
554 different extraction schemes, which can produce contrasting results for identical samples
555 (Tlustos et al., 2005); ii) the lack of either a universal standard or use of verified individual
556 mineral samples in all studies; and iii) verification that the extracted amount of Fe comes
557 from the intended target mineral phases. Poor siderite recovery by sequential extraction
558 procedures is a known issue (see references in Table 5), with yields ranging from < 2 % to
559 100 % using a variety of methods (Table 5). The recovery of other carbonates is similarly
560 variable and rarely reliably quantitative: 100 % for calcite; 98 % for ankerite; 45 – 95 % for
561 dolomite; 31 % for MnCO_3 and 12 % for rhodochrosite (Liu et al., 2018; Morera-Chavarria et
562 al., 2016; Raiswell et al., 1994).

563 MBS analysis of post-extract substrate in this study, revealed that siderite was not only
564 incompletely extracted during its target $\text{Fe}_{\text{aca-48}}$ stage (as previously noted by Reinhard et al.,
565 2009) but persisted throughout the entire procedure (Figs. 4 – 5). Even using Poulton and
566 Canfield's (2005) extended $\text{Fe}_{\text{aca-48}}$ procedure for crystalline siderite (48 hours at 50 °C,
567 rather than 24 hours at room temperature), we could only remove 3 – 8 % of the total Ivigtut
568 siderite Fe (with an average grain diameter of 16 μm , but a maximum diameter of 177 μm ,
569 measured by Fiji grain size analysis post pulverisation), which was significantly less than the
570 95 – 100 % yield of Roxbury and Biwabik siderite (both crushed to <63 μm) reported by

571 Poulton and Canfield (2005). It is possible that the reduced efficiency of Fe_{aca-48} for the
572 Ivigtut siderite, in comparison to that of the Roxbury or Biwabik siderite, was caused by the
573 presence of larger grains in the Ivigtut sample (Table 1 and Fig. 2a).

574 The Fe_{aca-48} extraction was further complicated by the apparent recovery of 30 % of the total
575 CARB-2 and CARB-3 Fe content (Table 4), both of which contain 30 % siderite. The
576 proportions of nontronite and 2-line ferrihydrite (Table 3) were also reduced in the CARB-2
577 (Fig. 4) and CARB-3 (Fig. 5) Fe_{aca-48} residue. The leachate Fe concentration implied
578 complete siderite removal in the target Fe_{aca-48} stage by, coincidentally, dissolving the same
579 amount of Fe from 2-line ferrihydrite and nontronite instead (Table 3, Figs. 4 – 5). As
580 mentioned in Section 2.4, the Fe_{aca-48} leach is only normally used in sequence on ancient
581 sediments, where ferrihydrite is unlikely to be present. The removal of 2-line ferrihydrite was
582 therefore not an unexpected result when using the more aggressive Fe_{aca-48} leach. Although
583 significant nontronite removal has been observed during Fe_{di-ct} (Raiswell et al. 1994), its
584 extraction during Fe_{aca-48} was unexpected, and may again be due to the longer, 48-hour leach
585 at 50 °C. Our main concern here was that, in isolation, the Fe_{aca-48} leach appeared to be
586 working, when clearly MBS shows that this was not the case.

587 2-line ferrihydrite was successfully removed by its target Fe_{hyam} stage, when present as an
588 individual mineral and as part of a mixture. The CARB-2 and CARB-3 Fe_{hyam} leachate
589 yielded less Fe than was expected, due to the removal of 2-line ferrihydrite during the
590 previous, Fe_{aca-48} stage.

591 The apparent recovery of 25 – 30 % (Table 4) of the total Fe available in CARB-2 and
592 CARB-3 (both of which contain approximately 20 % goethite) during Fe_{di-ct} , similarly
593 implied that all of the goethite Fe was dissolved (along with the partial dissolution of an/other

Extraction method	Yield	Complications	Reference
	95 – 100 %	Premature ferrihydrite	
	Fe _{aca-48} leachate [Fe] compared with Fe _{TOTAL} [Fe] via ICP-AAS	(3 %) and lepidocrocite (1 %) removal	(Poulton and Canfield, 2005)
1 M Na acetate pH 4.5 (acetic acid) 50 °C 48 hours	80 – 85 %	Incomplete siderite removal, 5 – 10 % passed onto following extraction stage	(Oonk et al., 2017)
	3 – 8 % Fe _{aca-48} leachate [Fe] compared with Fe _{TOTAL} [Fe] via ICP-AAS	Incomplete siderite removal Nontronite removal	This study
1 M Na acetate pH 5.0 (acetic acid) room temperature 5 hours	< 2 %	Efficiency of carbonate removal is strongly dependent on sample:reagent ratio	(Liu et al., 2018)
cold 10 % HCl room temperature 24 hours	0 – 16.3 %	Premature removal of 'easily reducible' oxides and silicates (NQ) Residual siderite partially removed by Fe _{oxa} extraction	(Raiswell et al., 2011; Reinhard et al., 2009)
0.5 M HCl 15 hours	NQ	Minute amounts of siderite remain	(Schröder et al., 2016)
chloroacetate/maleate buffer solutions pH ~ 0 80 °C 150 minutes	100 %	Requires at least 10 mg carbonate Not tested for use in sequential extraction (single stage only)	(Morera-Chavarria et al., 2016)

594 Table 5: Quantitative efficiency of modified Fe_{aca} extractions for siderite, compared with the original Poulton and Canfield
595 (2005) method. NQ = not quantified.

596 non-target mineral/s). According to the accompanying MBS spectrum, goethite was clearly
597 present in the Fe_{di-ct} residue, and that of the following Fe_{oxa} extraction (Figs. 4 – 5). It is
598 possible that a higher S:R ratio of 1.7 used in this study during Fe_{di-ct}, compared with the <
599 0.75 recommended by Thompson et al. (2019), may have been partially responsible for some
600 of the observed incomplete natural goethite extraction. However, the more successful
601 extraction of synthetic goethite at the same S:R (Table 3), implies that other factors (e.g.
602 grain size and matrix effects) were more likely to have caused the variable yields. Claff et al.
603 (2010) reported the remains of > 25 % goethite in residual samples even after an 8-hour
604 extraction and concluded that the dithionite extraction could not dissolve high concentrations
605 of crystalline Fe oxides (including akaganéite and haematite). Non-specificity and the post-
606 extraction re-adsorption of analytes onto residual solids can also cause variable results
607 depending on the substrate used (Kim et al., 2015; Bacon and Davidson, 2008; Hanahan,
608 2004). The almost complete removal of synthetic goethite Fe during its target Fe_{di-ct} stage
609 when run as an individual mineral (Table 2), but persistence in the residual CARB-2 mixture
610 (Fig. 4), suggests that matrix effects may be responsible for the variable goethite yields.

611 Magnetite was successfully targeted by Fe_{oxa} (Figs. 4 – 5) but the AAS leachate results reveal
612 that 28 – 69 % of the total magnetite Fe was also recovered during Fe_{di-ct} (Table 3). The
613 amount of magnetite dissolved in sodium dithionite in this study was much higher than the 5
614 – 7 % reported by Poulton and Canfield (2005) but matched that of Henkel et al. (2016) at 32
615 – 52 %. Premature magnetite dissolution was also observed by Schröder et al. (2016). All of
616 the Poulton and Canfield (2005) and some of the Henkel et al. (2016) Fe_{oxa} experiments, used
617 synthetic magnetite samples that were synthesised after Cornell and Schwertmann (2003).

618 Arbitrary behaviour of both nontronite samples was observed throughout the entire
619 procedure. As individual minerals, 50 – 56 % of the total NMS and NAu-2 nontronite Fe
620 contents were recovered as dithionite-extractable Fe (Table 3); the other non-target stages

621 yielded negligible ($< 6\%$) amounts (Table 3). Although this was higher than the 29% $\text{Fe}_{\text{di-ct}}$
622 recovery reported by Raiswell et al. (1994), the dissolution of nontronite Fe during $\text{Fe}_{\text{di-ct}}$ was
623 anticipated. However, MBS spectra of the individual mineral and the mixed Fe mineral
624 CARB-2 samples, showed that NMS nontronite was partially removed during $\text{Fe}_{\text{aca-48}}$ and
625 Fe_{hyam} , before its complete dissolution in Fe_{oxa} (Fig. 4). Dissolution and structural
626 modification of nontronite in Na acetate (Jaisi et al., 2008), HAHC (Ryan et al., 2008),
627 sodium dithionite (Jaisi et al., 2008), and ammonium oxalate (Wu et al., 2012) is known and
628 attributed to the reduction of structural Fe(III) (Borggaard, 1988). Conversely, the persistent
629 presence of NAu-2 at the end of each extraction, including the $\text{Fe}_{\text{HCl-1min}}$ stage, highlights the
630 operational nature of sequential extractions and their critical dependence on the specific
631 mineralogical composition of a sample. The Fe concentration measured during $\text{Fe}_{\text{aca-48}} - \text{Fe}_{\text{oxa}}$
632 may therefore be overestimated by the inclusion of non-target nontronite. The extra Fe
633 recovered from the CARB-2 and CARB-3 samples during Fe_{oxa} (Table 4) likely came from
634 the nontronite that was removed in Fe_{oxa} .

635 The changing shape of the NMS nontronite spectrum within the CARB-2 sample after each
636 consecutive extraction stage (Fig. 4), can be explained by the presence of Fe(III) in both the
637 octahedral and tetrahedral sheets of the nontronite crystal lattice. Significant ($> \sim 20\%$)
638 nontronite dissolution can cause irreversible dehydroxylation (Fialips et al., 2002) and
639 subsequent di-/trioctahedral substitution (Manceau et al., 2000) and partitioning of the
640 reagent-extracted Fe(II) into surface complexation and other reactive sites (Jaisi et al., 2008).
641 Preferential reduction of the dioctahedral sheet Fe(III) would result in a crystal structure
642 dominated by the remaining trioctahedral sheet Fe(III), and vice versa, changing the MBS
643 parameters and observed spectrum accordingly. Combined AAS leachate and MBS solid
644 residue observations for CARB-2, showed that approximately 45% of the NMS nontronite
645 Fe was removed during $\text{Fe}_{\text{aca-48}}$ (Fig. 6), which alone would be responsible for structural

646 modifications to the lattice structure. Re-adsorption of the extracted Fe(II) onto the nontronite
647 lattice may also explain why the changing shape of the NMS nontronite peak in the CARB-2
648 Mössbauer spectra between the Fe_{aca-48} and Fe_{hyam} extraction stages, was not also
649 accompanied by increased Fe concentrations in the NMS and NAu-2 leachates.

650 The recovery of synthetic goethite during Fe_{di-ct} in this study was greater than that of the
651 natural UoE goethite (Table 2). Sequential extraction procedures are generally applied on the
652 assumption that they target well-defined mineral phases, but natural samples often contain a
653 complex mixture of mineral phases that are not chemically or physically distinct (Kheboian
654 and Bauer, 1987). For example, the Fe speciation of natural mineral samples used in
655 sequential extraction procedures is often unknown, as is the interaction between the reactant
656 and specific solid Fe phases within the mineral matrix. However, this is exactly the
657 information that MBS can provide, to ensure the reliable comparison of data between
658 different sequential extraction experiments.

659 Poor reproducibility and non-selectivity of reactive Fe phases by wet chemical extraction has
660 been well known for some time, leading to the development of more aggressive dissolution
661 methods (e.g. for siderite, Table 5). Such alternative methods prove effective when used as
662 individual leaches but compromise subsequent extraction stages when used in sequence
663 (Raiswell et al., 1994). One such example is the room temperature extraction of siderite in
664 cold 10 % HCl for 24 hours, which simultaneously targets the 'easily-reducible' oxides
665 (Table 5). Premature removal of ferrihydrite and lepidocrocite does not restrict the
666 quantitative determination of Fe minerals in ancient sediment studies since the poorly-
667 ordered, nanoparticulate oxyhydroxide minerals are rapidly transformed into the more
668 thermodynamically-stable Fe mineral forms of goethite or haematite; ferrihydrite and
669 lepidocrocite are therefore not found in ancient sediments (Cornell and Schwertmann, 2003).
670 However, siderite, ferrihydrite, goethite, magnetite and nontronite are all important

671 constituents of modern sediments and their accurate quantitative identification is crucial for
672 understanding the diagenetic process that impact global Fe, C, P, and S cycling (Lal, 2008;
673 Cooper et al., 2005; Cooper et al., 2000; Kostka and Luther, 1994), the speciation and
674 mobility of metals that contaminate natural environments (Jonsson and Sherman, 2008; Guo
675 et al., 2007; Fendorf et al., 2000; Fredrickson et al., 2000; Lovley, 1993), and even the
676 storage of radioactive waste (Hu et al., 2019; Ithurbide et al., 2010; Scheinost and Charlet,
677 2008).

678 The strength of any sequential extraction technique depends on the specific solubility of a
679 particular mineral phase in a well-defined reagent. Incomplete, premature, and non-selective
680 dissolution of target minerals exemplifies the importance of using an additional analytical
681 technique to identify the residual phases at each stage of the procedure. The reported
682 specificity of the sequential Fe extraction (Poulton and Canfield, 2005) cannot be assumed
683 for all samples. When used in isolation, without careful calibration of the reacting Fe mineral
684 phases, the sequential extraction could present entirely misleading information for the
685 determination of specific Fe-containing minerals. Verification of the extracted or residual
686 phases is therefore crucial for the correct interpretation of the leachate results.

687 Examples of secondary analyses used to verify the Fe minerals or mineral groups present in
688 the extracted leachate or the residual material, include MBS (Jilbert et al., 2018; Sun et al.,
689 2018; Schröder et al., 2016), LA-ICP-MS (Oonk et al., 2018), SEM or TEM (Xie et al., 2018;
690 Zhuang et al., 2012), XAS (Sun et al., 2018; Barber et al., 2017), tests with ⁵⁸Fe isotope
691 spiking (Henkel et al. 2016), or a percentage yield comparison from a single mineral control
692 or internal laboratory standard (Jin et al., 2018; Liu et al., 2018; Lynch et al., 2018; Qi et al.,
693 2018; Lei et al., 2017; Oonk et al., 2017; Xie et al., 2017; Raiswell et al., 2010). The
694 advantage of MBS is the ability to analyse a sample non-destructively and in a single, short
695 step without additional preparation. XRD offers another suitable alternative for the

696 mineralogical characterisation of reactive Fe minerals when Co radiation (Mos et al., 2018)
697 or a monochromator (Fransen, 2004) is used to repress fluorescence. However, X-ray
698 diffractometers are rarely suitably configured for the classification of reactive Fe minerals.
699 Although some of the verification techniques that are listed here are costly and not always
700 readily available, there is little excuse not to run appropriate pure mineral standards alongside
701 the extracted samples.

702 **4.2 Implications for use with modern and ancient sediments**

703 The implications of using data from unverified extractions, depend entirely upon the way in
704 which it is interpreted. In ancient rocks and sediments that are diagenetically stabilised, the
705 Poulton and Canfield (2005) chemical extraction is simply applied to compare the sum of
706 highly reactive Fe (Fe-bound carbonates, oxides, magnetite, and pyrite) with that of total Fe,
707 to distinguish oxic/euxinic from anoxic depositional conditions (Poulton et al., 2004). In fact,
708 the Poulton and Canfield (2005) technique was specifically designed for this purpose.

709 Although the results of our study highlight some severe reliability issues with mineral
710 specificity at individual stages, palaeoceanographic reconstructions of the water column only
711 attempt to quantify the fraction of sediment Fe that is reactive towards sulphide (Berner,
712 1984, 1970). Since a mineral specific interpretation is not required, the non-specific removal
713 of individual Fe phases observed at specific stages of a sequential extraction is unlikely to
714 alter the conclusions of work that employs sediment Fe as a palaeoredox proxy. Furthermore,
715 in many such studies, Fe palaeoredox data are used in combination with other
716 palaeoenvironmental proxies to develop a picture of the evolving system.

717 Isotopic or trace metal analyses alternatively require the successful isolation of a specific
718 mineral phase (e.g. carbonate), rather than an operationally-defined phase (e.g. Na acetate-
719 extractable). Here, the Fe content of the leachate may only represent a small portion of the
720 target mineral phase. As a purely hypothetical example, if less than half of the goethite and

721 other reducible iron oxides/oxyhydroxides are actually targeted during the Fe_{di-ct} reduction
722 (Table 2 and Table 3), the estimated preservation of $19 - 45 \times 10^{15}$ g of OC in surface marine
723 sediments (Lalonde et al., 2012), and the impact of Fe in global C sequestration, would be
724 severely underestimated. Studies based solely on the chemical extraction of Fe in modern
725 sediments that assume a mineral-specific approach are most likely to be affected by
726 inconsistent or erroneous outcomes of leaching methods.

727 Our work reiterates many of the limitations that have already been raised regarding the
728 sequential extraction method for Fe (Poulton and Canfield, 2005). The incomplete extraction
729 of siderite and goethite were respectively reported by Reinhard et al. (2009) and Claff et al.
730 (2010). Both Schröder et al. (2016) and Henkel et al. (2016) documented the premature
731 removal of magnetite, while Raiswell et al. (1994) demonstrated the extensive dissolution of
732 nontronite prior to Fe_{HCl} . Our observation of premature ferrihydrite extraction during Fe_{aca-48}
733 was also not surprising, since the 48-hour Na acetate leach at 50 °C is rarely used to extract
734 siderite in samples where ferrihydrite is present. Furthermore, Poulton and Canfield (2005)
735 reported the premature removal of small amounts of ferrihydrite (during the 24-hour Fe_{aca}
736 stage) and magnetite (during the Fe_{di-ct} stage) in their original paper. In spite of such
737 warnings, the Poulton and Canfield (2005) method continues to be used for mineral-specific
738 analyses – a purpose for which it was not originally designed. Where sequential extractions
739 are used to define specific mineral phases, we strongly advise that i) all leachate results are
740 verified by a secondary, independent means of analysis and ii) the operational nature of
741 extraction techniques is clearly defined.

742

743

5. CONCLUSIONS

744 The novel comparison of MBS residue and ICP-AAS leachate analyses at each stage in the
745 Poulton and Canfield (2005) procedure, raises key concerns as to the reliable use of
746 sequential extraction protocols for Fe mineral identification in mineral-specific applications.
747 Our analyses use synthetic minerals produced according to Cornell and Schwertmann (2003),
748 as in the original Poulton and Canfield (2005) method. Incomplete and premature dissolution
749 of target minerals throughout the procedure affects the subsequent extraction stages.
750 Unverified interpretations of the leachate Fe content are particularly misleading where the
751 solubilised Fe is not the intended target phase. Matrix effects and grain size greatly affect the
752 precision of individual extraction stages between natural and synthetic forms of the same
753 mineral, between different natural samples of the same mineral, and even between identical
754 samples. In fact, the behaviour of Fe minerals in the extraction method is clearly more
755 dependent on the property of the mineral than the specific mineral itself. Poor precision and
756 reliability are ultimately due to the operational nature of the technique, which is
757 misunderstood or ignored in the majority of the research that employs the extraction for
758 mineral-specific purposes.

759 MBS is a powerful tool with advantages over x-ray-based techniques, most notably the
760 accurate characterisation of amorphous colloidal and nanoparticulate Fe minerals. The
761 combined use of MBS alongside conventional sequential extraction procedures can provide a
762 reliable means of semi-quantitative Fe mineral identification that is suitable for mineral
763 specific applications in studies of both modern and ancient sediments.

764

765

ACKNOWLEDGMENTS

766 This work was supported by the Carnegie Trust for the Universities of Scotland through a
767 Collaborative Research Grant (Trust Reference No: 50357). The authors acknowledge the
768 generous XRD-based expertise of Peter Davidson at National Museums Scotland, and

769 Anthony Oldroyd at Cardiff University, who have been integral to this work. Thanks are also
770 due to Alastair Tait for photomicrograph production. The authors thank Simon Poulton,
771 Susann Henkel, and an anonymous reviewer for their helpful comments, which improved the
772 original manuscript.

773

774

REFERENCES

- 775 Adamo, P., Agrelli, D. and Zampella, M. (2018) Chapter 9 - chemical speciation to assess
776 bioavailability, bioaccessibility and geochemical forms of potentially toxic metals
777 (PTMs) in polluted soils. In *Environmental Geochemistry*, second ed. (eds. B. De
778 Vivo, H. E. Belkin, A. Lima). Elsevier (2018). pp 153-194.
779 <http://dx.doi.org/10.1016/B978-0-444-63763-5.00010-0>.
- 780 Afonso M. D. and Stumm W. (1992) Reductive dissolution of iron(III) (hydr)oxides by
781 hydrogen sulfide. *Langmuir* **8**, 1671-1675. <https://doi.org/10.1021/la00042a030>.
- 782 Bacon J. R. and Davidson C. M. (2008) Is there a future for sequential chemical extraction?
783 *Analyst* **133**, 25-46. <https://doi.org/10.1039/B711896A>.
- 784 Baeyens W., Monteny F., Leermakers M. and Bouillon S. (2003) Evaluation of sequential
785 extractions on dry and wet sediments. *Anal. Bioanal. Chem.* **376**, 890-901.
786 <https://doi.org/10.1007/s00216-003-2005-z>.
- 787 Barber A., Brandes J., Leri A., Lalonde K., Balind K., Wirick S., Wang J. and Gélinas Y.
788 (2017) Preservation of organic matter in marine sediments by inner-sphere
789 interactions with reactive iron. *Sci. Rep.-UK* **7**, 366. [https://doi.org/10.1038/s41598-](https://doi.org/10.1038/s41598-017-00494-0)
790 [017-00494-0](https://doi.org/10.1038/s41598-017-00494-0).
- 791 Berner R. A. (1970) Sedimentary pyrite formation. *Am. J. Sci.* **268**, 1-23.
792 <https://doi.org/10.2475/ajs.268.1.1>.

793 Berner R. A. (1984) Sedimentary pyrite formation - an update. *Geochim. Cosmochim. Acta*
794 **48**, 605-615. [https://doi.org/10.1016/0016-7037\(84\)90089-9](https://doi.org/10.1016/0016-7037(84)90089-9).

795 Blonder B., Boyko V., Turchyn A.V., Antler G., Sinichkin U., Knossow N., Klein R. and
796 Kamyshny A. (2017) Impact of aeolian dry deposition of reactive iron minerals on
797 sulfur cycling in sediments of the Gulf of Aqaba. *Front. Microbiol.* **8**, 1131.
798 <https://doi.org/10.3389/fmicb.2017.01131>.

799 Borggaard O.K. (1988) Phase identification by phase dissolution techniques. In *Iron in soils*
800 *and clay minerals* NATO ASI Series (Series C: Mathematical and Physical Sciences),
801 vol 217 (eds. J. W. Stucki, B. A. Goodman, U. Schwertmann). Springer, Dordrecht.
802 pp. 83-98. https://doi.org/10.1007/978-94-009-4007-9_5.

803 Brindley G. W. (1980) Order-disorder in clay mineral structures. In *Crystal structures of clay*
804 *minerals and their x-ray identification* (eds G. W. Brindley and G. Brown).
805 Mineralogical Society, London. pp. 125-195. <https://doi.org/10.1180/mono-5.2>.

806 Canfield D. E. (1989) Reactive iron in marine sediments. *Geochim Cosmochim Acta* **53**, 619-
807 632. [https://doi.org/10.1016/0016-7037\(89\)90005-7](https://doi.org/10.1016/0016-7037(89)90005-7).

808 Canfield D. E., Poulton S. W. and Narbonne G. M. (2007) Late-Neoproterozoic deep-ocean
809 oxygenation and the rise of animal life. *Science* **315**, 92-95.
810 <https://doi.org/10.1126/science.1135013>.

811 Chen X., Ling H. F., Vance D., Shields-Zhou G. A., Zhu M. Y., Poulton S. W., Och L. M.,
812 Jiang S. Y., Li D., Cremonese L. and Archer C. (2015) Rise to modern levels of ocean
813 oxygenation coincided with the Cambrian radiation of animals. *Nat. Commun.* **6**,
814 7142. <https://doi.org/10.1038/ncomms8142>.

815 Claff S. R., Sullivan L. A., Burton E. D. and Bush R. T. (2010) A sequential extraction
816 procedure for acid sulfate soils: partitioning of iron. *Geoderma* **155**, 224-230.
817 <https://doi.org/10.1016/j.geoderma.2009.12.002>.

818 Cooper D. C., Neal A. L., Kukkadapu R. K., Brewe D., Coby A. and Picardal F. W. (2005)
819 Effects of sediment iron mineral composition on microbially mediated changes in
820 divalent metal speciation: importance of ferrihydrite. *Geochim. Cosmochim. Acta* **69**,
821 1739-1754. <https://doi.org/10.1016/j.gca.2004.09.013>.

822 Cooper D. C., Picardal F., Rivera J. and Talbot C. (2000) Zinc immobilization and magnetite
823 formation via ferric oxide reduction by *Shewanella putrefaciens* 200. *Environ. Sci.*
824 *Technol.* **34**, 100-106. <https://doi.org/10.1021/es990510x>.

825 Cornell R. M. and Schwertmann U. (2003) Synthesis. In *The iron oxides: structure,*
826 *properties, reactions, occurrences and uses* (eds. R. M. Cornell and U.
827 Schwertmann). WILEY-VCH Verlag GmbH & Co. KGaA, Weinheim. pp. 527-542.
828 <https://doi.org/10.1002/3527602097.ch20>.

829 Dahl T. W., Hammarlund E. U., Anbar A. D., Bond D. P. G., Gill B. C., Gordon G. W.,
830 Knoll A. H., Nielsen A. T., Schovsbo N. H. and Canfield D. E. (2010) Devonian rise
831 in atmospheric oxygen correlated to the radiations of terrestrial plants and large
832 predatory fish. *P. Natl. Acad. Sci. USA* **107**, 17911-17915.
833 <https://doi.org/10.1073/pnas.1011287107>.

834 Dijkstra N., Slomp C. P., Behrends T. and Expedition 347 Scientists (2016) Vivianite is a key
835 sink for phosphorus in sediments of the Landsort Deep, an intermittently anoxic deep
836 basin in the Baltic Sea. *Chem. Geol.* **438**, 58-72.
837 <https://doi.org/10.1016/j.chemgeo.2016.05.025>.

838 Ding S., Wang Y., Wang D., Li Y. Y., Gong M. and Zhang C. (2016) In situ, high-resolution
839 evidence for iron-coupled mobilization of phosphorus in sediments. *Sci. Rep.-UK* **6**,
840 24341. <https://doi.org/10.1038/srep24341>.

841 Eiche E., Kramar U., Berg M., Berner Z., Norra S. and Neumann T. (2010) Geochemical
842 changes in individual sediment grains during sequential arsenic extractions. *Water*
843 *Res.* **44**, 5545-5555. <https://doi.org/10.1016/j.watres.2010.06.002>.

844 Estes E. R., Pockalny R., D'Hondt S., Inagaki F., Morono Y., Murray R. W., Nordlund D.,
845 Spivack A. J., Wankel S. D., Xiao N. and Hansel C. M. (2019) Persistent organic
846 matter in oxic subseafloor sediment. *Nat. Geosci.* **12**, 126-131.
847 <https://doi.org/10.1038/s41561-018-0291-5>.

848 Fendorf S., Wielinga B. W. and Hansel C. M. (2000) Chromium transformations in natural
849 environments: the role of biological and abiological processes in chromium(VI)
850 reduction. *Int. Geol. Rev.* **42**, 691-701. <https://doi.org/10.1080/00206810009465107>.

851 Fialips C. I., Huo D. F., Yan L. B., Wu J. and Stucki J. W. (2002) Effect of Fe oxidation state
852 on the IR spectra of Garfield nontronite. *Am. Mineral.* **87**, 630-641.
853 <https://doi.org/10.2138/am-2002-5-605>.

854 Fransen, M. J. (2004) 1- and 2-dimensional detection systems and the problem of sample
855 fluorescence in x-ray diffractometry. *Adv X-ray Anal.* **47**, 224–231.

856 Fredrickson J. K., Zachara J. M., Kennedy D. W., Duff M. C., Gorby Y. A., Li S.M.W. and
857 Krupka K. M. (2000) Reduction of U(VI) in goethite (alpha-FeOOH) suspensions by
858 a dissimilatory metal-reducing bacterium. *Geochim. Cosmochim. Acta* **64**, 3085-3098.
859 [https://doi.org/10.1016/S0016-7037\(00\)00397-5](https://doi.org/10.1016/S0016-7037(00)00397-5).

860 Ghaisas N. A., Maiti K. and White J. R. (2019) Coupled iron and phosphorus release from
861 seasonally hypoxic Louisiana shelf sediment. *Estuar. Coast. Shelf S.* **219**, 81-89.
862 <https://doi.org/10.1016/j.ecss.2019.01.019>.

863 Gobeil C., Johnson W. K., Macdonald R. W. and Wong C. S. (1995) Sources and burden of
864 lead in St. Lawrence estuary sediments – isotopic evidence. *Environ. Sci. & Technol.*
865 **29**, 193-201. <https://doi.org/10.1021/es00001a025>.

866 Gómez-Ariza, J. L., Giráldez, I., Sánchez-Rodas, D. and Morales, E. (1999) Metal
867 readsorption and redistribution during the analytical fractionation of trace elements in
868 oxic estuarine sediments. *Anal. Chim. Acta* **399**, 295-307.
869 [https://doi.org/10.1016/S0003-2670\(99\)00460-2](https://doi.org/10.1016/S0003-2670(99)00460-2).

870 Guilbaud R., Butler I. B., Ellam R. M. and Rickard, D. (2010) Fe isotope exchange between
871 Fe(II)_{aq} and nanoparticulate mackinawite (FeS_m) during nanoparticle growth. *Earth*
872 *Planet. Sc. Lett.* **300**, 174-183. <https://doi.org/10.1016/j.epsl.2010.10.004>.

873 Guo H. M., Stüben D. and Berner Z. (2007) Removal of arsenic from aqueous solution by
874 natural siderite and hematite. *Appl. Geochem.* **22**, 1039-1051.
875 <https://doi.org/10.1016/j.apgeochem.2007.01.004>.

876 Gütlich P. and Schröder C. (2012) Mössbauer spectroscopy. In *Methods in Physical*
877 *Chemistry* (eds. R. Schäfer and P. C. Schmidt). Wiley-VCH, Weinheim. pp. 351-389.
878 <https://doi.org/10.1002/9783527636839.ch11>.

879 Haese R. R., Wallmann K., Dahmke A., Kretzmann U., Müller P. J. and Schulz H.D. (1997)
880 Iron species determination to investigate early diagenetic reactivity in marine
881 sediments. *Geochim. Cosmochim. Acta* **61**, 63-72. [https://doi.org/10.1016/S0016-](https://doi.org/10.1016/S0016-7037(96)00312-2)
882 [7037\(96\)00312-2](https://doi.org/10.1016/S0016-7037(96)00312-2).

883 Hammarlund E. U., Smith M. P., Rasmussen J. A., Nielsen A. T., Canfield D. E. and Harper
884 D. A. T. (2019) The Sirius Passet Lagerstätte of North Greenland—geochemical
885 window on early Cambrian low-oxygen environments and ecosystems. *Geobiology*
886 **17**, 12-26. <https://doi.org/10.1111/gbi.12315>.

887 Hanahan C. (2004) Dissolution of hydroxide minerals in the 1 M sodium acetate, pH 5,
888 extracting solution in sequential extraction schemes. *Environ. Geol.* **45**, 864-868.
889 <https://doi.org/10.1007/s00254-003-0946-3>.

890 Hass A. and Fine P. (2010) Sequential selective extraction procedures for the study of heavy
891 metals in soils, sediments, and waste materials—a critical review. *Crit. Rev. Env. Sci.*
892 *Tec.* **40**, 365-399. <https://doi.org/10.1080/10643380802377992>.

893 Henkel S., Kasten S., Poulton S. W. and Staubwasser M. (2016) Determination of the stable
894 iron isotopic composition of sequentially leached iron phases in marine sediments.
895 *Chem. Geol.* **421**, 93-102. <https://doi.org/10.1016/j.chemgeo.2015.12.003>.

896 Henkel S., Kasten S., Hartmann J. F., Silva-Busso A. and Staubwasser M. (2018) Iron
897 cycling and stable Fe isotope fractionation in Antarctic shelf sediments, King George
898 Island. *Geochim. Cosmochim. Acta* **237**, 320-338.
899 <https://doi.org/10.1016/j.gca.2018.06.042>.

900 Heron G., Crouzet C., Bourg A. C. M. and Christensen T. H. (1994) Speciation of Fe(II) and
901 Fe(III) in contaminated aquifer sediments using chemical extraction techniques.
902 *Environ. Sci. Tech.* **28**, 1698-1705. <https://doi.org/10.1021/es00058a023>.

903 Homoky W. B., John S. G., Conway T. M. and Mills R. A. (2013) Distinct iron isotopic
904 signatures and supply from marine sediment dissolution. *Nat. Commun.* **4**, 2143.
905 <https://doi.org/10.1038/ncomms3143>.

906 Hu W., Zhang Z. X., Li M. X., Liu H. B., Zhang C. G., Chen T. H. and Zhou Y. F. (2019)
907 Enhanced uptake capacity for uranium(VI) in aqueous solutions by activated natural
908 siderite: performance and mechanism. *Appl. Geochem.* **100**, 96-103.
909 <https://doi.org/10.1016/j.apgeochem.2018.11.010>.

910 Ithurbide A., Peulon S., Miserque F., Beaucaire C. and Chaussé, A. (2010) Retention and
911 redox behaviour of uranium(VI) by siderite (FeCO₃). *Radiochim. Acta* **98**, 563-568.
912 <https://doi.org/10.1524/ract.2010.1754>.

913 Jaisi D. P., Dong H. L. and Morton J. P. (2008) Partitioning of Fe(II) in reduced nontronite
914 (NAu-2) to reactive sites: reactivity in terms of Tc(VII) reduction. *Clay. Clay Miner.*
915 **56**, 175-189. <https://doi.org/10.1346/CCMN.2008.0560204>.

916 Jilbert T., Asmala E., Schröder C., Tiihonen R., Myllykangas J. P., Virtasalo J. J., Kotilainen
917 A., Peltola P., Ekholm P. and Hietanen S. (2018) Impacts of flocculation on the
918 distribution and diagenesis of iron in boreal estuarine sediments. *Biogeosciences* **15**,
919 1243-1271. <https://doi.org/10.5194/bg-15-1243-2018>.

920 Jin C. S., Li C., Algeo T. J., O'Connell B., Cheng M., Shi W., Shen J. and Planavsky N. J.
921 (2018) Highly heterogeneous "poikiloredox" conditions in the early Ediacaran
922 Yangtze Sea. *Precambrian Res.* **311**, 157-166.
923 <https://doi.org/10.1016/j.precamres.2018.04.012>.

924 Jönsson J. and Sherman D. M. (2008) Sorption of As(III) and As(V) to siderite, green rust
925 (fougerite) and magnetite: implications for arsenic release in anoxic groundwaters.
926 *Chem. Geol.* **255**, 173-181. <https://doi.org/10.1016/j.chemgeo.2008.06.036>.

927 Keil R. G., Montlucon D. B., Prahel F. G. and Hedges J. I. (1994) Sorptive preservation of
928 labile organic matter in marine sediments. *Nature* **370**, 549-552.
929 <https://doi.org/10.1038/370549a0>.

930 Kersten M., Garbe-Schönberg C. D., Thomsen S., Anagnostou C. and Sioulas A. (1997)
931 Source apportionment of Pb pollution in the coastal waters of Elefsis Bay, Greece.
932 *Environ. Sci. Technol.* **31**, 1295-1301. <https://doi.org/10.1021/es960473z>.

933 Kheboian C. and Bauer C. F. (1987) Accuracy of selective extraction procedures for metal
934 speciation in model aquatic sediments. *Anal. Chem.* **59**, 1417-1423.
935 <https://doi.org/10.1021/ac00137a010>.

936 Kim E. J., Lee J. C. and Baek K. (2015) Abiotic reductive extraction of arsenic from
937 contaminated soils enhanced by complexation: arsenic extraction by reducing agents

938 and combination of reducing and chelating agents. *J. Hazard. Mater.* **283**, 454-461.
939 <https://doi.org/10.1016/j.jhazmat.2014.09.055>.

940 Kostka J. E. and Luther III G. W. (1994) Partitioning and speciation of solid-phase iron in
941 salt marsh sediments. *Geochim. Cosmochim. Acta* **58**, 1701-1710.
942 [https://doi.org/10.1016/0016-7037\(94\)90531-2](https://doi.org/10.1016/0016-7037(94)90531-2).

943 Kraal P., Dijkstra N., Behrends T. and Slomp C. P. (2017) Phosphorus burial in sediments of
944 the sulfidic deep Black Sea: key roles for adsorption by calcium carbonate and apatite
945 authigenesis. *Geochim. Cosmochim. Acta* **204**, 140-158.
946 <https://doi.org/10.1016/j.gca.2017.01.042>.

947 Lal R. (2008) Sequestration of atmospheric CO₂ in global carbon pools. *Energ. Environ. Sci.*
948 **1**, 86-100. <https://doi.org/10.1039/B809492F>.

949 Lalonde K., Mucci A., Ouellet A. and G elinas Y. (2012) Preservation of organic matter in
950 sediments promoted by iron. *Nature* **483**, 198-200.
951 <https://doi.org/10.1038/nature10855>.

952 Lei L.-D., Shen J., Li C., Algeo T. J., Chen Z.-Q., Feng Q.-L., Cheng M., Jin C.-S. and
953 Huang J.-H. (2017) Controls on regional marine redox evolution during Permian-
954 Triassic transition in South China. *Palaeogeogr. Palaeoclimatol. Palaeoecol.* **486**, 17-
955 32. <https://doi.org/10.1016/j.palaeo.2017.02.010>.

956 Lenstra W. K., Egger M., van Helmond N. A. G. M., Kritzberg E., Conley D. J. and Slomp C.
957 P. (2018) Variations in iron input to an oligotrophic Baltic Sea estuary: impact on
958 sedimentary phosphorus burial. *Biogeosciences* **15**, 6979-6996.
959 <https://doi.org/10.5194/bg-15-6979-2018>.

960 Li J., Zhang Y. and Katsev S. (2018) Phosphorus recycling in deeply oxygenated sediments
961 in Lake Superior controlled by organic matter mineralization. *Limnol. Oceanogr.* **63**,
962 1372-1385. <https://doi.org/10.1002/lno.10778>.

963 Liu Y., Zhang J. and He H. (2018) Assessment of the Tessier and BCR sequential extraction
964 procedures for elemental partitioning of Ca, Fe, Mn, Al, and Ti and their application
965 to surface sediments from Chinese continental shelf. *Acta Oceanol. Sin.* **37**, 22-28.
966 <https://doi.org/10.1007/s13131-018-1189-1>.

967 Lovley D. R. (1993) Dissilatory metal reduction. *Annu. Rev. Microbiol.* **47**, 263-290.
968 [10.1146/annurev.mi.47.100193.001403](https://doi.org/10.1146/annurev.mi.47.100193.001403).

969 Lynch S. F. L., Batty L. C. and Byrne P. (2018) Environmental risk of severely Pb-
970 contaminated riverbank sediment as a consequence of hydrometeorological
971 perturbation. *Sci. Total Environ.* **636**, 1428-1441.
972 <https://doi.org/10.1016/j.scitotenv.2018.04.368>.

973 Mos Y. M., Vermeulen A. C., Buisman C. J. N. and Weijma J. (2018) X-ray diffraction of
974 iron containing samples: the importance of a suitable configuration. *Geomicrobiol. J.*
975 **35**, 511-517. <https://doi.org/10.1080/01490451.2017.1401183>.

976 Ma W.-W., Zhu M.-X., Yang G.-P. and Li, T. (2017) In situ, high-resolution DGT
977 measurements of dissolved sulfide, iron and phosphorus in sediments of the East
978 China Sea: insights into phosphorus mobilization and microbial iron reduction. *Mar.*
979 *Pollut. Bull.* **124**, 400-410. <https://doi.org/10.1016/j.marpolbul.2017.07.056>.

980 Ma W.-W., Zhu M.-X., Yang G.-P. and Li T. (2018) Iron geochemistry and organic carbon
981 preservation by iron (oxyhydr)oxides in surface sediments of the East China Sea and
982 the south Yellow Sea. *J. Marine Syst.* **178**, 62-74.
983 <https://doi.org/10.1016/j.jmarsys.2017.10.009>.

984 Manceau A., Drits V. A., Lanson B., Chateigner D., Wu J., Huo D., Gates W. P. and Stucki J.
985 W. (2000) Oxidation-reduction mechanism of iron in dioctahedral smectites: II.
986 Crystal chemistry of reduced Garfield nontronite. *Am. Mineral.* **85**, 153-172.
987 <https://doi.org/10.2138/am-2000-0115>.

988 Markussen T. N., Elberling B., Winter C. and Andersen T. J. (2016) Flocculated meltwater
989 particles control Arctic land-sea fluxes of labile iron. *Sci. Rep.-UK* **6**, 24033.
990 <https://doi.org/10.1038/srep24033>.

991 Mayer L. M. (1994) Surface area control of organic carbon accumulation in continental shelf
992 sediments. *Geochim. Cosmochim. Acta* **58**, 1271-1284. [https://doi.org/10.1016/0016-](https://doi.org/10.1016/0016-7037(94)90381-6)
993 [7037\(94\)90381-6](https://doi.org/10.1016/0016-7037(94)90381-6).

994 Morera-Chavarría A., Griffioen J. and Behrends T. (2016) Optimized sequential extraction
995 for carbonates: quantification and $\delta^{13}\text{C}$ analysis of calcite, dolomite and siderite.
996 *Chem. Geol.* **443**, 146-157. <https://doi.org/10.1016/j.chemgeo.2016.09.025>.

997 Nemati K., Bakar N. K. A., Abas M. R. and Sobhazadeh E. (2009) Concentration
998 measurement and evaluation of mobility of heavy metals of Zayandeh-Rood river
999 sediments. *Asian J. Chem.* **21**, 4894-4900.

1000 Oonk P. B. H., Mason P. R. D., Tsikos H. and Bau M. (2018) Fraction-specific rare earth
1001 elements enable the reconstruction of primary seawater signatures from iron
1002 formations. *Geochim. Cosmochim. Acta* **238**, 102-122.
1003 <https://doi.org/10.1016/j.gca.2018.07.005>.

1004 Oonk P. B. H., Tsikos H., Mason P. R. D., Henkel S., Staubwasser M., Fryer L., Poulton S.
1005 W. and Williams H.M. (2017) Fraction-specific controls on the trace element
1006 distribution in iron formations: implications for trace metal stable isotope proxies.
1007 *Chem. Geol.* **474**, 17-32. <https://doi.org/10.1016/j.chemgeo.2017.10.018>.

1008 Parat C., Lévêque J., Dousset S., Chaussod R. and Andreux F. (2003) Comparison of three
1009 sequential extraction procedures used to study trace metal distribution in an acidic
1010 sandy soil. *Anal. Bioanal. Chem.* **376**, 243-247. [https://doi.org/10.1007/s00216-003-](https://doi.org/10.1007/s00216-003-1864-7)
1011 [1864-7](https://doi.org/10.1007/s00216-003-1864-7).

1012 Peter S. and Sobek S. (2018) High variability in iron-bound organic carbon among five
1013 boreal lake sediments. *Biogeochemistry* **139**, 19-29. [https://doi.org/10.1007/s10533-](https://doi.org/10.1007/s10533-018-0456-8)
1014 [018-0456-8](https://doi.org/10.1007/s10533-018-0456-8).

1015 Posth N. R., Köhler I., Swanner E. D., Schröder C., Wellmann E., Binder B., Konhauser K.
1016 O., Neumann U., Berthold C., Nowak M. and Kappler A. (2013) Simulating
1017 Precambrian banded iron formation diagenesis. *Chem. Geol.* **362**, 66-73.
1018 <https://doi.org/10.1016/j.chemgeo.2013.05.031>.

1019 Poulton S. W. and Canfield D. E. (2005) Development of a sequential extraction procedure
1020 for iron: implications for iron partitioning in continentally derived particulates. *Chem.*
1021 *Geol.* **214**, 209-221. <https://doi.org/10.1016/j.chemgeo.2004.09.003>.

1022 Poulton S. W., Fralick P. W. and Canfield D. E. (2004) The transition to a sulphidic ocean
1023 similar to 1.84 billion years ago. *Nature* **431**, 173-177.
1024 <https://doi.org/10.1038/nature02912>.

1025 Qi C., Li C., Gabbott S. E., Ma X., Xie L., Deng W., Jin C. and Hou X.-G. (2018) Influence
1026 of redox conditions on animal distribution and soft-bodied fossil preservation of the
1027 Lower Cambrian Chengjiang Biota. *Palaeogeogr. Palaeoclimatol. Palaeoecol.* **507**,
1028 180-187. <https://doi.org/10.1016/j.palaeo.2018.07.010>.

1029 Raiswell R., Benning L. G., Tranter M. and Tulaczyk S. (2008) Bioavailable iron in the
1030 Southern Ocean: the significance of the iceberg conveyor belt. *Geochem T.* **9**, 7.
1031 <https://doi.org/10.1186/1467-4866-9-7>.

1032 Raiswell R. and Canfield D. E. (1996) Rates of reaction between silicate iron and dissolved
1033 sulfide in Peru Margin sediments. *Geochim. Cosmochim. Acta* **60**, 2777-2787.
1034 [https://doi.org/10.1016/0016-7037\(96\)00141-X](https://doi.org/10.1016/0016-7037(96)00141-X).

1035 Raiswell R., Canfield D. E. and Berner R. A. (1994) A comparison of iron extraction
1036 methods for the determination of degree of pyritisation and the recognition of iron-

1037 limited pyrite formation. *Chem. Geol.* **111**, 101-110. <https://doi.org/10.1016/0009->
1038 2541(94)90084-1.

1039 Raiswell R., Reinhard C. T., Derkowski A., Owens J., Bottrell S. H., Anbar A. D. and Lyons
1040 T. W. (2011) Formation of syngenetic and early diagenetic iron minerals in the late
1041 Archean Mt. McRae Shale, Hamersley Basin, Australia: new insights on the patterns,
1042 controls and paleoenvironmental implications of authigenic mineral formation.
1043 *Geochim. Cosmochim. Acta* **75**, 1072-1087. <https://doi.org/10.1016/j.gca.2010.11.013>.

1044 Raiswell R., Vu H. P., Brinza L. and Benning L. G. (2010) The determination of labile Fe in
1045 ferrihydrite by ascorbic acid extraction: methodology, dissolution kinetics and loss of
1046 solubility with age and de-watering. *Chem. Geol.* **278**, 70-79.
1047 <https://doi.org/10.1016/j.chemgeo.2010.09.002>.

1048 Rancourt D. G. and Ping J. Y. (1991) Voigt-based methods for arbitrary-shape static
1049 hyperfine parameter distributions in Mössbauer spectroscopy. *Nucl. Instrum. Meth. B*
1050 **58**, 85-97. [https://doi.org/10.1016/0168-583X\(91\)95681-3](https://doi.org/10.1016/0168-583X(91)95681-3).

1051 Ransom B., Kim D., Kastner M. and Wainwright S. (1998) Organic matter preservation on
1052 continental slopes: importance of mineralogy and surface area. *Geochim. Cosmochim.*
1053 *Acta* **62**, 1329-1345. [https://doi.org/10.1016/S0016-7037\(98\)00050-7](https://doi.org/10.1016/S0016-7037(98)00050-7).

1054 Reinhard C. T., Raiswell R., Scott C., Anbar A. D. and Lyons T. W. (2009) A late Archean
1055 sulfidic sea stimulated by early oxidative weathering of the continents. *Science* **326**,
1056 713-716. <https://doi.org/10.1126/science.1176711>.

1057 Ryan P. C., Hillier S. and Wall A. J. (2008) Stepwise effects of the BCR sequential chemical
1058 extraction procedure on dissolution and metal release from common ferromagnesian
1059 clay minerals: a combined solution chemistry and X-ray powder diffraction study. *Sci.*
1060 *Total Environ.* **407**, 603-614. <https://doi.org/10.1016/j.scitotenv.2008.09.019>.

1061 Sahuquillo A., López-Sánchez, J. F., Rubio R., Rauret G., Thomas R. P., Davidson C. M. and
1062 Ure A. M. (1999) Use of a certified reference material for extractable trace metals to
1063 assess sources of uncertainty in the BCR three-stage sequential extraction procedure.
1064 *Anal. Chim. Acta* **382**, 317-327. [https://doi.org/10.1016/S0003-2670\(98\)00754-5](https://doi.org/10.1016/S0003-2670(98)00754-5).

1065 Sanchez-Espana J. and Reyes J. (2019) Comparing schwertmannite and hydrobasaluminite
1066 dissolution in ammonium oxalate (pH 3.0): implications for metal speciation studies
1067 by sequential extraction. *Minerals* **9**, 57. <https://doi.org/10.3390/min9010057>.

1068 Scheinost A. C. and Charlet L. (2008) Selenite reduction by mackinawite, magnetite and
1069 siderite: XAS characterization of nanosized redox products. *Environ. Sci. Technol.* **42**,
1070 1984-1989. <https://doi.org/10.1021/es071573f>.

1071 Schindelin J., Arganda-Carreras I., Frise E., Kaynig V., Longair M., Pietzsch T., Preibisch S.,
1072 Preibisch S., Rueden C., Saalfeld S., Schmid B., Tinevez J. Y., White D. J.,
1073 Hartenstein V., Eliceiri K., Tomancak P. and Cardona A. (2012) Fiji: an open source
1074 platform for biological-image analysis. *Nat. Methods* **9**, 676 - 682.
1075 <https://doi.org/10.1038/nmeth.2019>.

1076 Scholz F., Severmann S., McManus J., Noffke A., Lomnitz U. and Hensen C. (2014) On the
1077 isotope composition of reactive iron in marine sediments: redox shuttle versus early
1078 diagenesis. *Chem. Geol.* **389**, 48-59. <https://doi.org/10.1016/j.chemgeo.2014.09.009>.

1079 Schröder C., Köhler I., Müller, F. L. L., Chumakov A. I., Kuppenko I., Ruffer R. and Kappler
1080 A. (2016) The biogeochemical iron cycle and astrobiology. *Hyperfine Interact.* **237**,
1081 85. <https://doi.org/10.1007/s10751-016-1289-2>.

1082 Severmann S., McManus J., Berelson W. M. and Hammond D. E. (2010) The continental
1083 shelf benthic iron flux and its isotope composition. *Geochim. Cosmochim. Acta* **74**,
1084 3984-4004. <https://doi.org/10.1016/j.gca.2010.04.022>.

1085 Sulkowski M. and Hirner A. V. (2006) Element fractionation by sequential extraction in a
1086 soil with high carbonate content. *Appl. Geochem.* **21**, 16-28.
1087 <https://doi.org/10.1016/j.apgeochem.2005.09.016>.

1088 Sun J., Mailloux B. J., Chillrud S. N., van Geen A., Thompson A. and Bostick B. C. (2018)
1089 Simultaneously quantifying ferrihydrite and goethite in natural sediments using the
1090 method of standard additions with X-ray absorption spectroscopy. *Chem. Geol.* **476**,
1091 248-259. <https://doi.org/10.1016/j.chemgeo.2017.11.021>.

1092 Sutherland R. A. (2010) BCR (R)-701: a review of 10-years of sequential extraction analyses.
1093 *Anal. Chim. Acta* **680**, 10-20. <https://doi.org/10.1016/j.aca.2010.09.016>.

1094 Thompson J., Poulton S. W., Guilbaud R., Doyle K. A., Reid S. and Krom M.D. (2019).
1095 Development of a modified SEDEX phosphorus speciation method for ancient rocks
1096 and modern iron-rich sediments. *Chem. Geol.* **524**, 383-393.
1097 <https://doi.org/10.1016/j.chemgeo.2019.07.003>

1098 Tlustoš P., Száková J., Stárková A. and Pavlíková D. (2005) A comparison of sequential
1099 extraction procedures for fractionation of arsenic, cadmium, lead, and zinc in soil.
1100 *Cent. Eur. J. Chem.* **3**, 830-851. <https://doi.org/10.2478/BF02475207>.

1101 Ure A. M. (1991) Trace element speciation in soils, soil extracts and solutions. *Microchim.*
1102 *Acta* **104**, 49. <https://doi.org/10.1007/BF01245495>.

1103 Wallmann K., Hennies K., König I., Petersen, W. and Knauth H. D. (1993) New procedure
1104 for determining reactive Fe(III) and Fe(II) minerals in sediments. *Limnol. Oceanogr.*
1105 **38**, 1803-1812. <https://doi.org/10.4319/lo.1993.38.8.1803>.

1106 Weber F.-A., Voegelin A. and Kretzschmar R. (2009) Multi-metal contaminant dynamics in
1107 temporarily flooded soil under sulfate limitation. *Geochim. Cosmochim. Acta* **73**,
1108 5513-5527. <https://doi.org/10.1016/j.gca.2009.06.011>.

- 1109 Wehrmann L. M., Riedinger N., Brunner B., Kamyshny Jr. A., Hubert C. R. J., Herbert L. C.,
1110 Brüchert, V., Jørgensen B. B., Ferdelman T. G. and Formolo M. J. (2017) Iron-
1111 controlled oxidative sulfur cycling recorded in the distribution and isotopic
1112 composition of sulfur species in glacially influenced fjord sediments of west Svalbard.
1113 *Chem. Geol.* **466**, 678-695. <https://doi.org/10.1016/j.chemgeo.2017.06.013>.
- 1114 Whalley C. and Grant, A. (1994) Assessment of the phase selectivity of the European
1115 Community Bureau of Reference (BCR) sequential extraction procedure for metals in
1116 sediment. *Anal. Chim. Acta* **291**, 287-295. [https://doi.org/10.1016/0003-](https://doi.org/10.1016/0003-2670(94)80024-3)
1117 [2670\(94\)80024-3](https://doi.org/10.1016/0003-2670(94)80024-3).
- 1118 Wu T., Shelobolina E., Xu H. F., Konishi H., Kukkadapu R. and Roden E. E. (2012) Isolation
1119 and microbial reduction of Fe(III) phyllosilicates from subsurface sediments. *Environ.*
1120 *Sci. Technol.* **46**, 11618-11626. <https://doi.org/10.1021/es302639n>.
- 1121 Xie Y., Lu G., Yang C., Qu L., Chen M., Guo C. and Dang Z. (2018) Mineralogical
1122 characteristics of sediments and heavy metal mobilization along a river watershed
1123 affected by acid mine drainage. *Plos One* **13**, e0190010.
1124 <https://doi.org/10.1371/journal.pone.0190010>.
- 1125 Xie Y., Lu G., Ye H., Yang C., Xia D., Yi X., Reinfelder J. and Dang Z. (2017) Fulvic acid
1126 induced the liberation of chromium from CrO₄²⁻-substituted schwertmannite. *Chem.*
1127 *Geol.* **475**, 52-61. <https://doi.org/10.1016/j.chemgeo.2017.10.031>.
- 1128 Zhuang Y.-F., Fialips C. I., White M. L. and Ferrandez D. M. P. (2012) New redox-active
1129 material for permeable water remediation systems. *Appl. Clay Sci.* **59-60**, 26-35.
1130 <https://doi.org/10.1016/j.clay.2012.02.002>.
- 1131 Zimmerman, A. J. and Weindorf, D. C. (2010) Heavy metal and trace metal analysis in soil
1132 by sequential extraction: a review of procedures. *Int. J. Anal. Chem.* **2010**, 387803.
1133 <https://doi.org/10.1155/2010/387803>.

1134
1135
1136
1137
1138
1139
1140
1141
1142
1143
1144
1145
1146
1147
1148
1149
1150

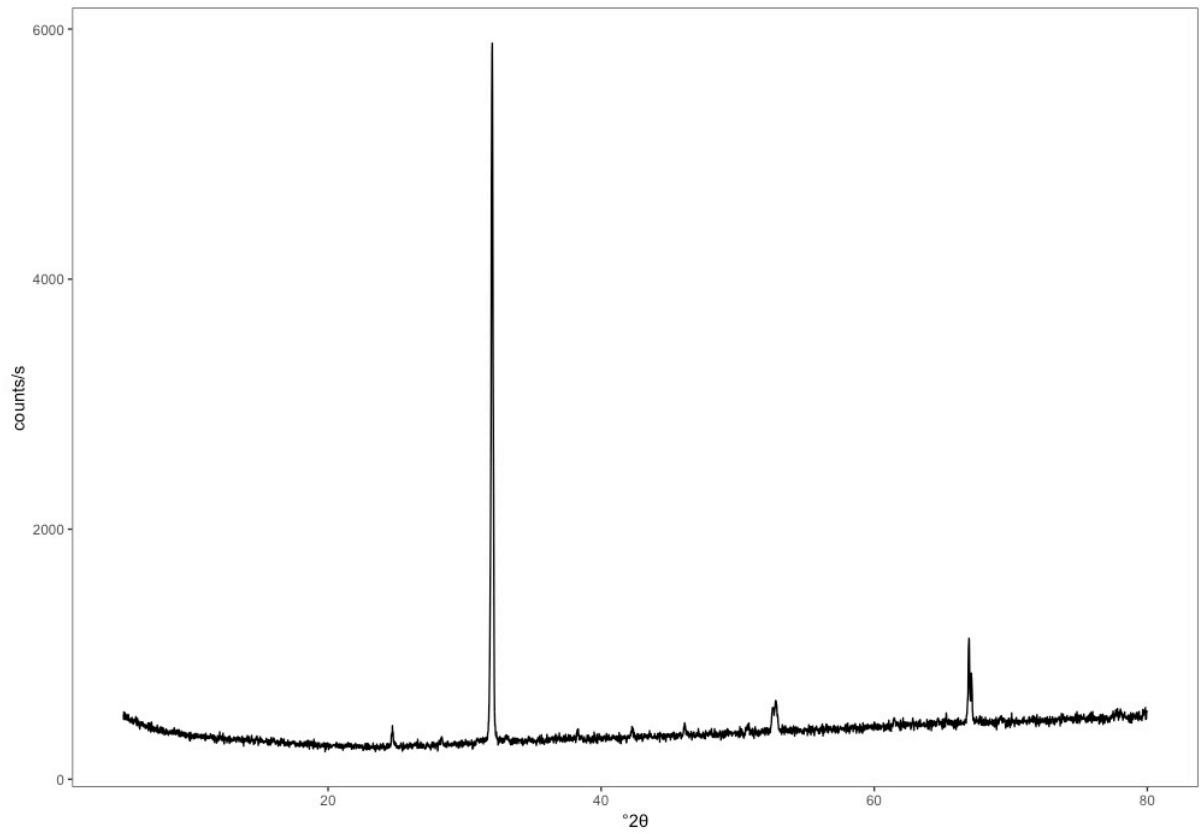
Appendix A to

**The use of operationally-defined sequential Fe extraction methods
for mineralogical applications: a cautionary tale from Mössbauer
spectroscopy**

Laura E. Hepburn, Ian B. Butler, Adrian Boyce, Christian Schröder

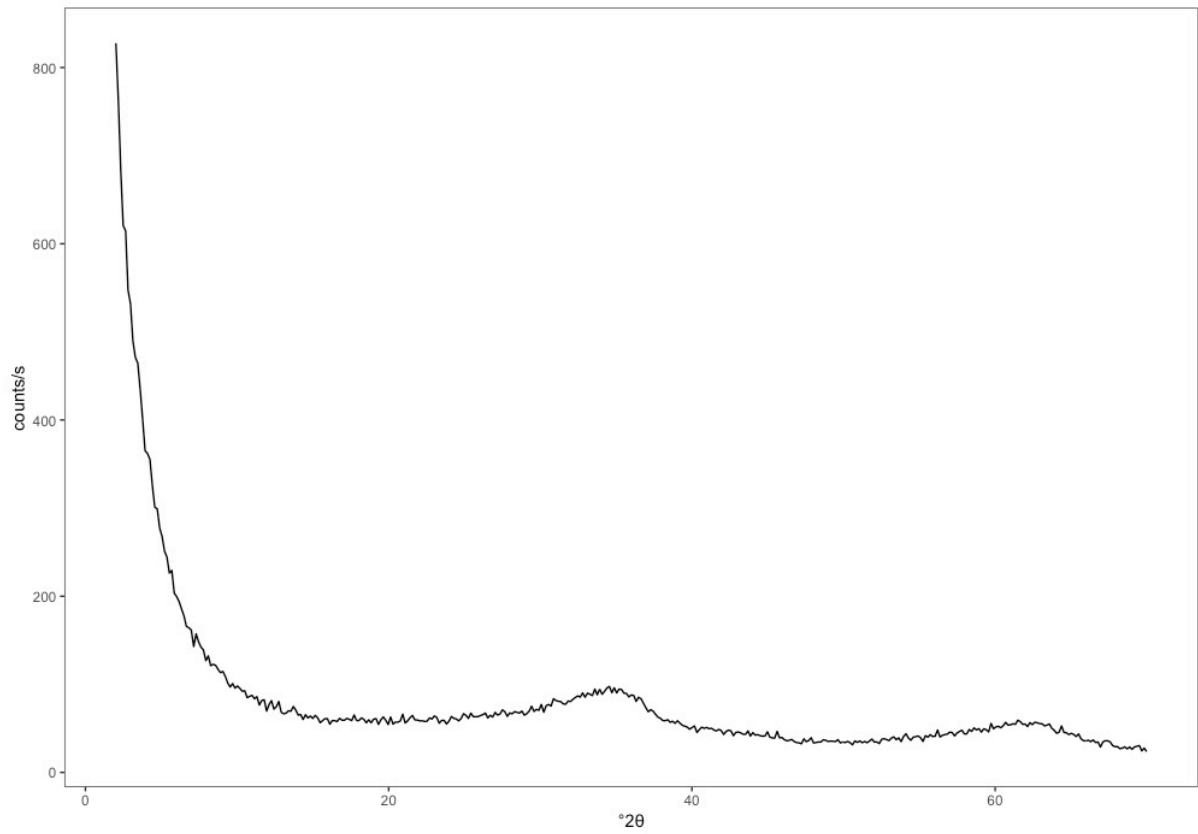
Content

- Figure A1:** Unleached natural Ivigtut siderite XRD spectrum.
- Figure A2:** Unleached synthetic 2-line ferrihydrite XRD spectrum.
- Figure A3:** Unleached synthetic goethite XRD spectrum.
- Figure A4:** Unleached natural UoE goethite XRD spectrum.
- Figure A5:** Unleached synthetic magnetite XRD spectrum.
- Figure A6:** Unleached natural NMS nontronite XRD spectrum.
- Figure A7:** Unleached natural NAu-2 nontronite XRD spectrum.



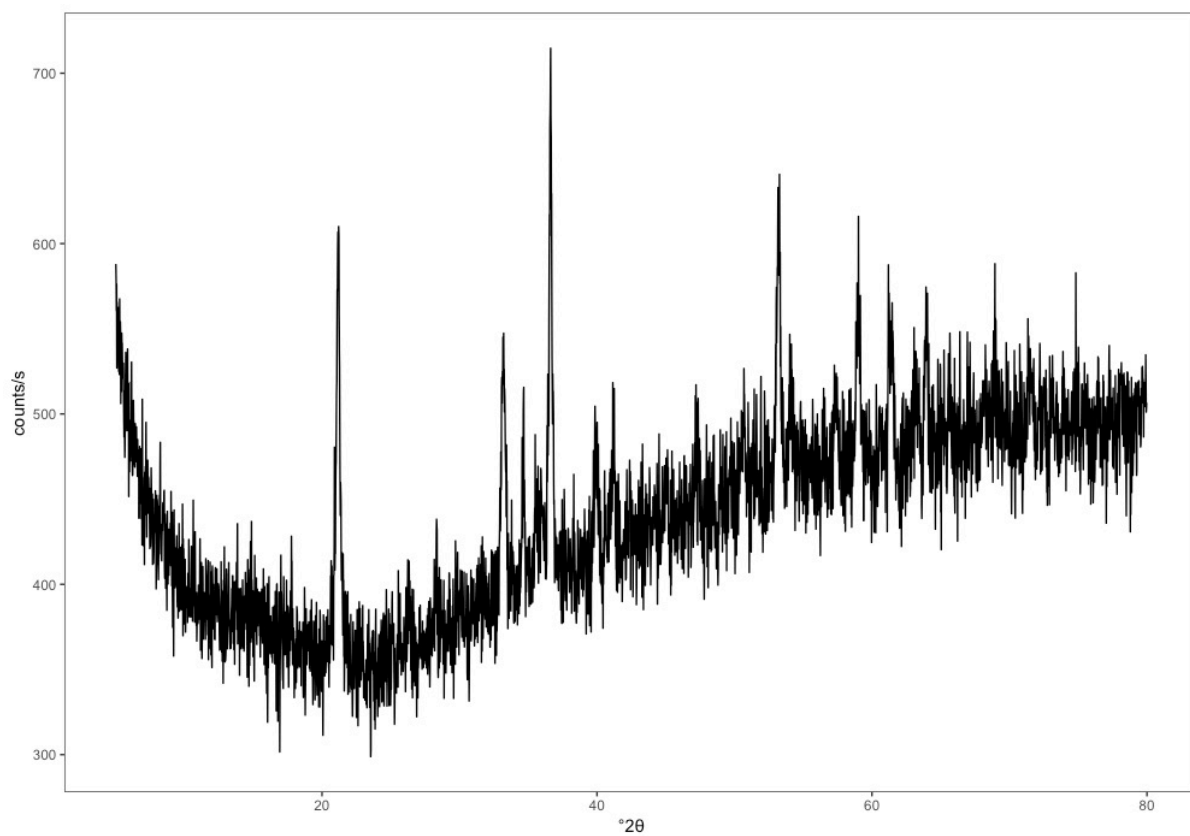
1151

1152 *Figure A1: Unleached natural Ivigtut siderite XRD spectrum. CuK α radiation without*
1153 *monochromator, National Museums Collection Centre, Edinburgh, UK.*



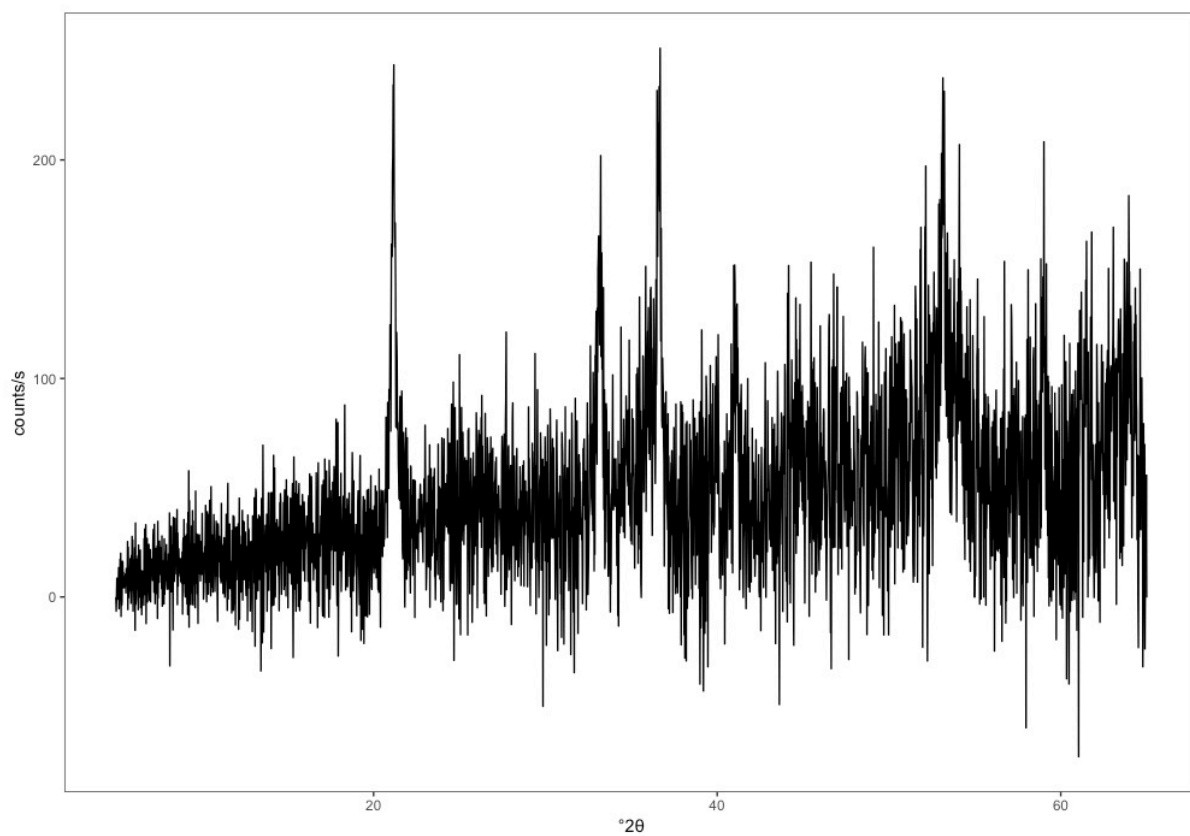
1154

1155 *Figure A2: Unleached synthetic 2-line ferrihydrite XRD spectrum. CuK α radiation with*
1156 *monochromator, Cardiff University, UK.*



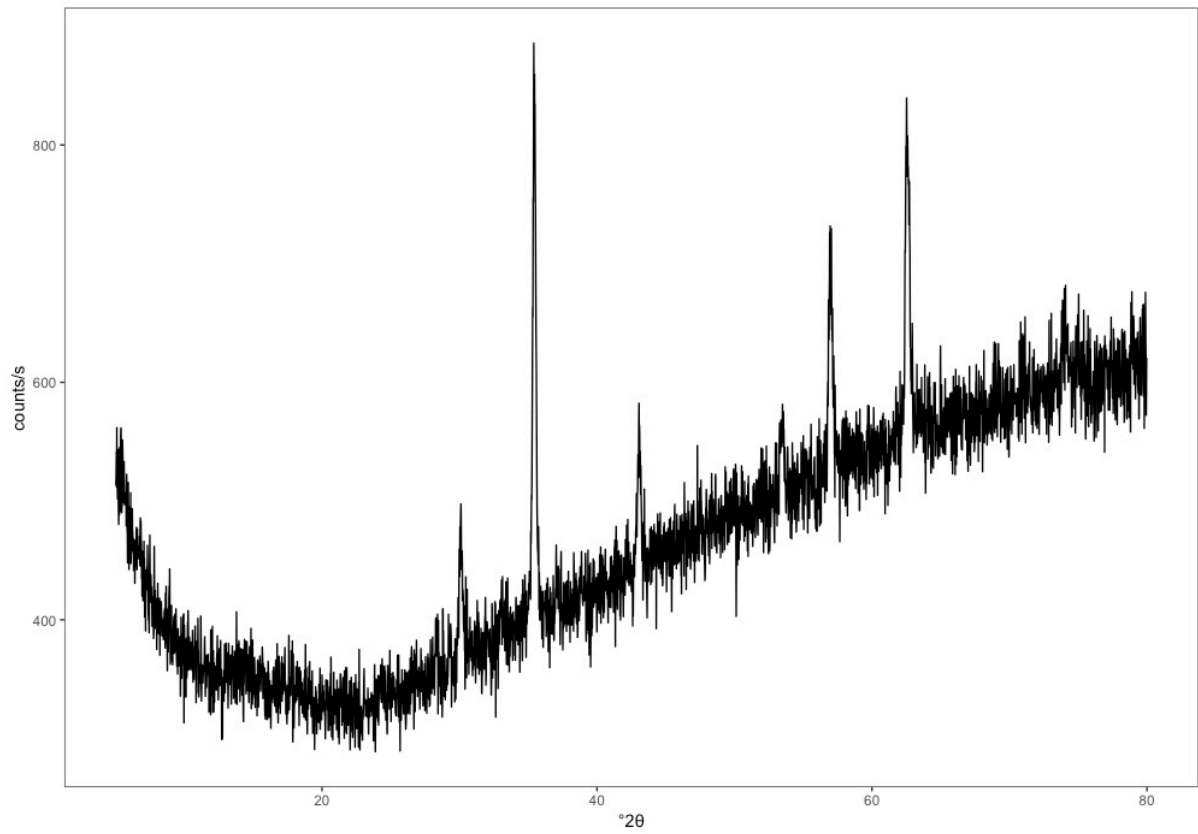
1157

1158 *Figure A3: Unleached synthetic goethite XRD spectrum. CuK α radiation without*
1159 *monochromator, National Museums Collection Centre, Edinburgh, UK.*



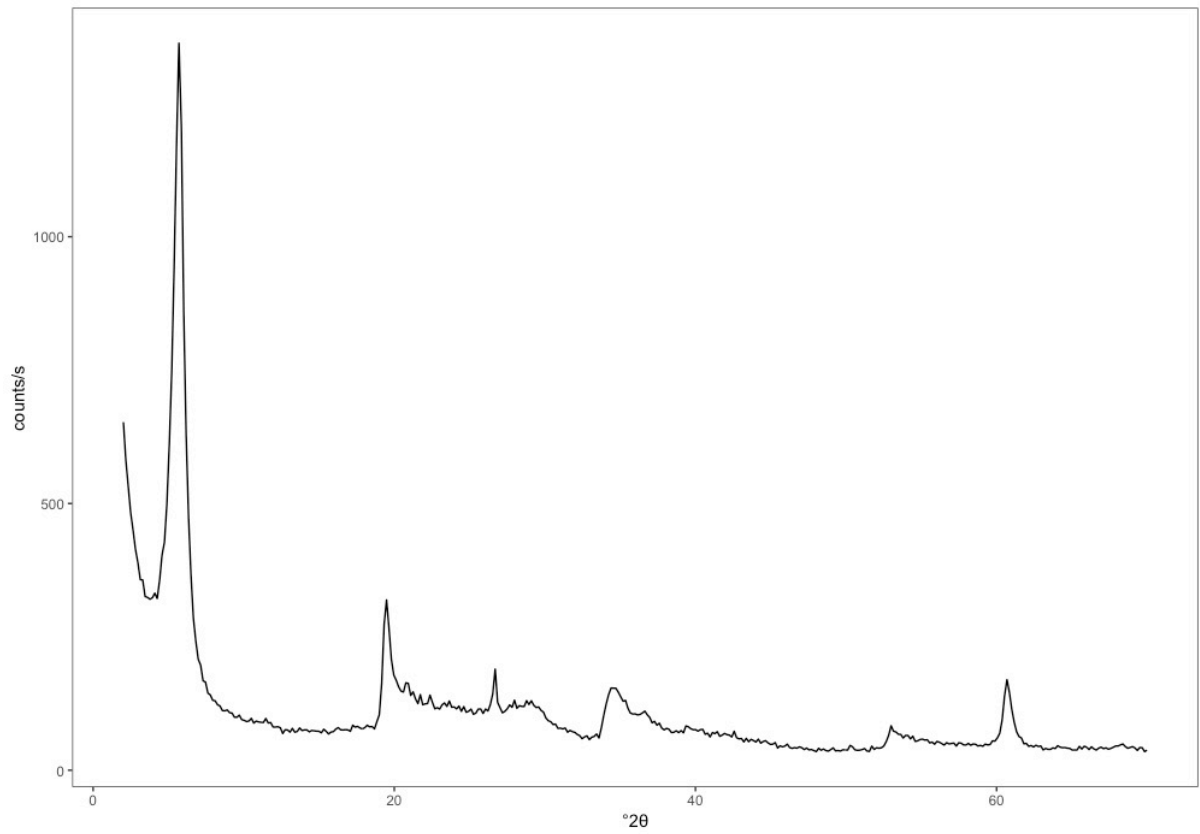
1160

1161 *Figure A4: Unleached natural UoE goethite XRD spectrum. CuK α radiation without*
1162 *monochromator, University of Edinburgh, UK.*



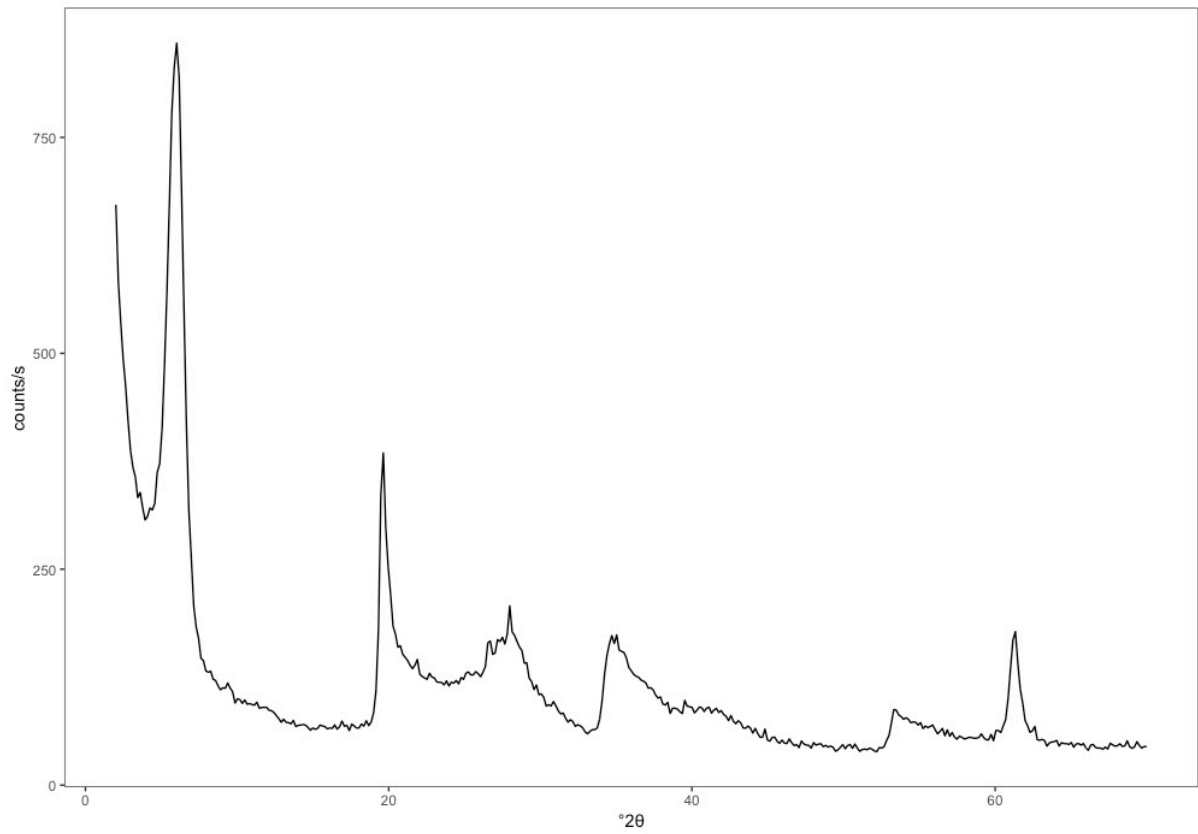
1163

1164 *Figure A5: Unleached synthetic magnetite XRD spectrum. CuK α radiation without*
1165 *monochromator, National Museums Collection Centre, Edinburgh, UK.*



1166

1167 *Figure A6: Unleached natural NMS nontronite XRD spectrum. CuK α radiation with*
1168 *monochromator, Cardiff University, UK.*



1169

1170 *Figure A7: Unleached natural NAu-2 nontronite XRD spectrum. CuK α radiation with*
1171 *monochromator, Cardiff University, UK.*

1172 **Appendix B to**

1173

1174 **The use of operationally-defined sequential Fe extraction methods**
1175 **for mineralogical applications: a cautionary tale from Mössbauer**
1176 **spectroscopy**

1177

1178 *Laura E. Hepburn, Ian B. Butler, Adrian Boyce, Christian Schröder*

1179

1180

1181 **Content**

1182 **Figure B8:** Observed and fitted Mössbauer spectroscopy spectrum for the unleached natural Ivigtut
1183 siderite sample used in this study.

1184 **Figure B9:** Observed and fitted Mössbauer spectroscopy spectrum for the unleached synthetic 2-line
1185 ferrihydrite sample used in this study.

1186 **Figure B10:** Observed and fitted Mössbauer spectroscopy spectrum for the unleached synthetic
1187 goethite sample used in this study.

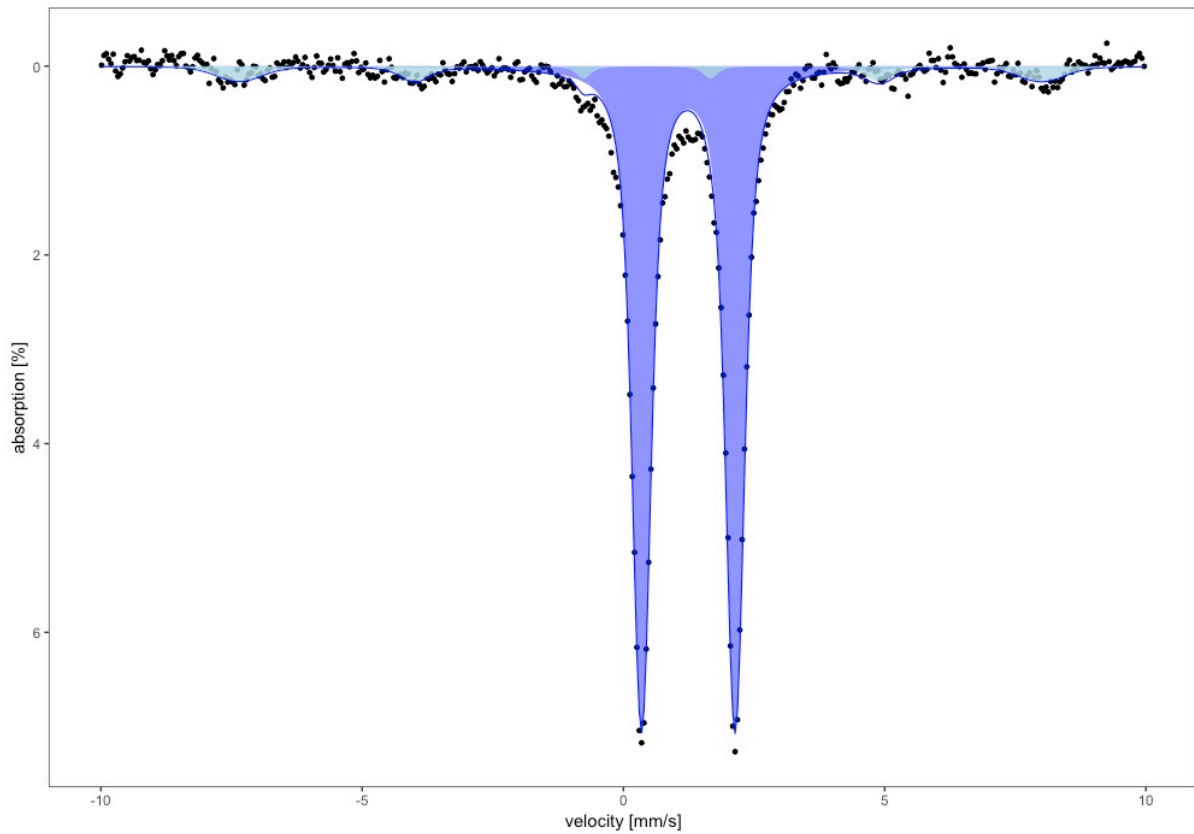
1188 **Figure B11:** Observed and fitted Mössbauer spectroscopy spectrum for the unleached natural UoE
1189 goethite sample used in this study.

1190 **Figure B12:** Observed and fitted Mössbauer spectroscopy spectrum for the unleached synthetic
1191 magnetite sample used in this study.

1192 **Figure B13:** Observed and fitted Mössbauer spectroscopy spectrum for the unleached natural NMS
1193 nontronite sample used in this study.

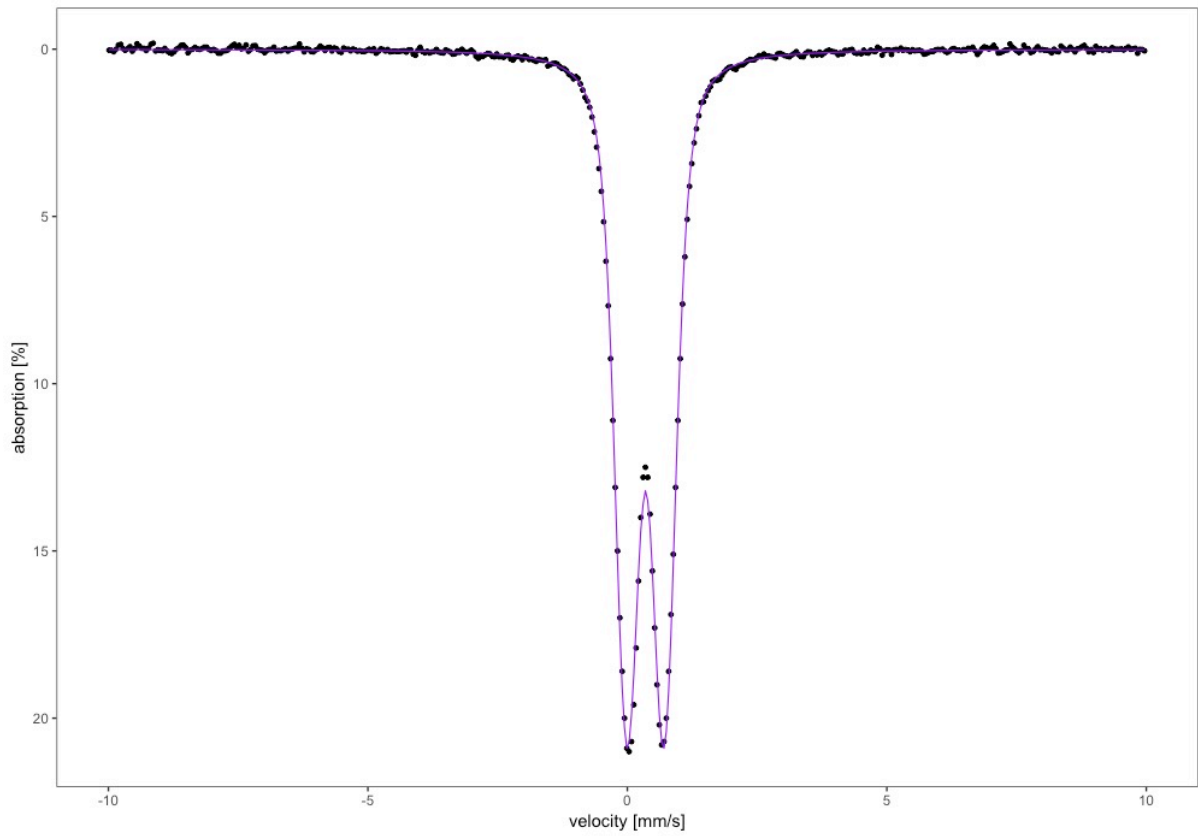
1194 **Figure B14:** Observed and fitted Mössbauer spectroscopy spectrum for the unleached natural NAu-2
1195 nontronite sample used in this study.

1196



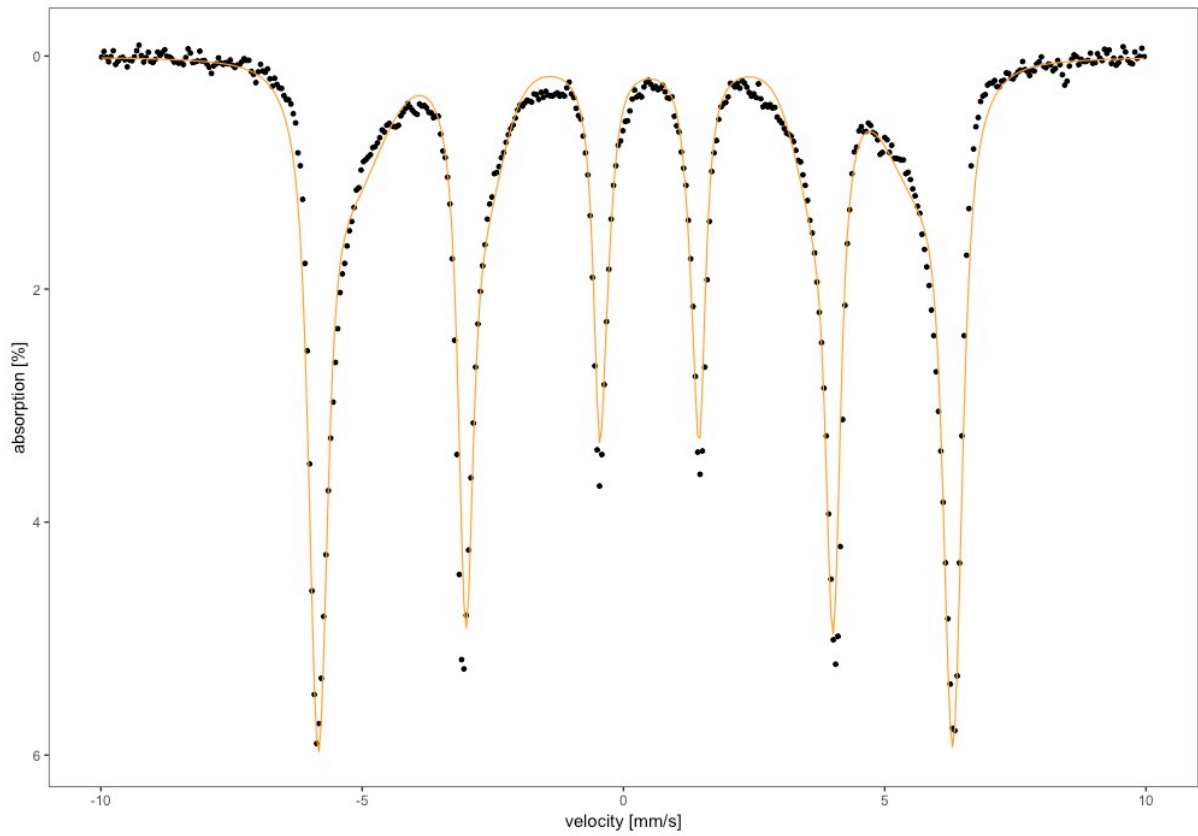
1197

1198 *Figure B8: Observed (black circles) and fitted (blue line) Mössbauer spectroscopy spectrum*
1199 *for the unleached natural Ivigtut siderite sample used in this study. The dark blue-filled area*
1200 *is the typical Fe²⁺ siderite signature. The light blue-filled area represents Fe³⁺ in an iron oxide*
1201 *phase of low crystallinity and shows that a small amount of the iron in Ivigtut siderite is*
1202 *oxidised.*



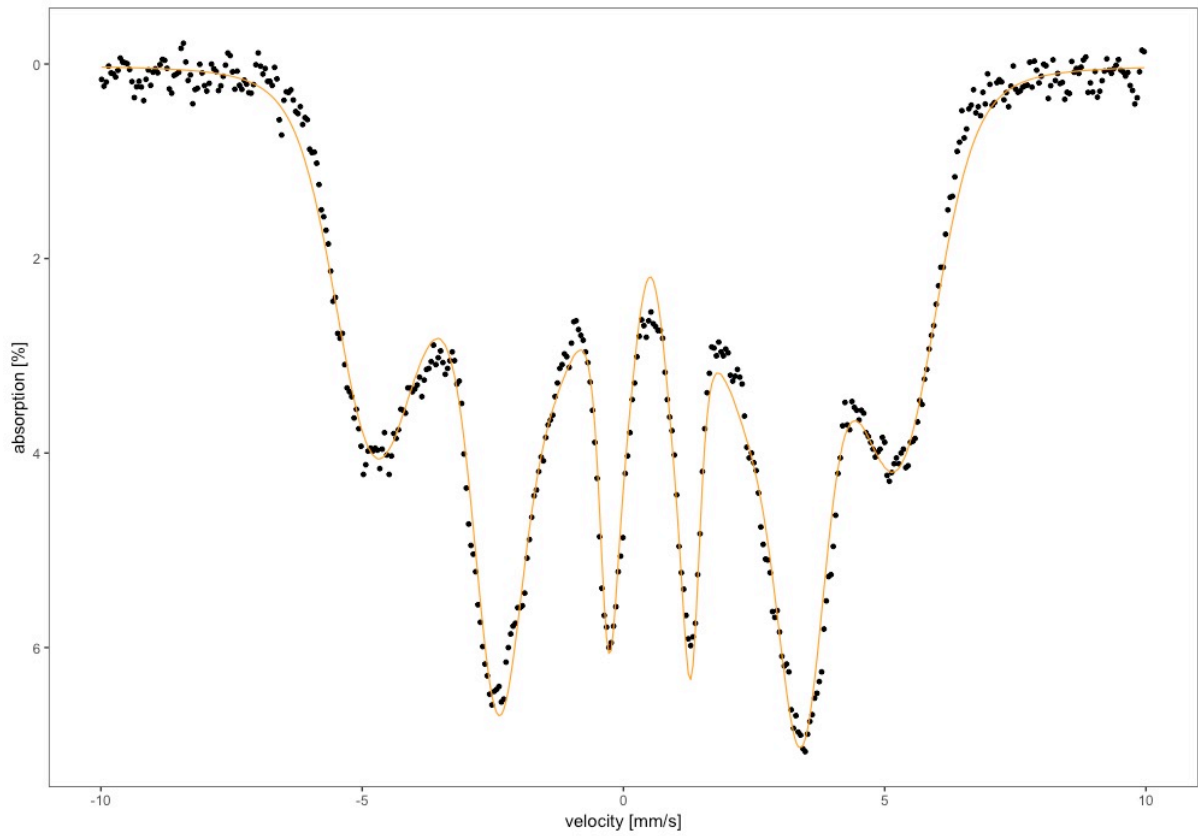
1203

1204 *Figure B9: Observed (black circles) and fitted (purple line) Mössbauer spectroscopy spectrum*
1205 *for the unleached synthetic 2-line ferrihydrite sample used in this study.*



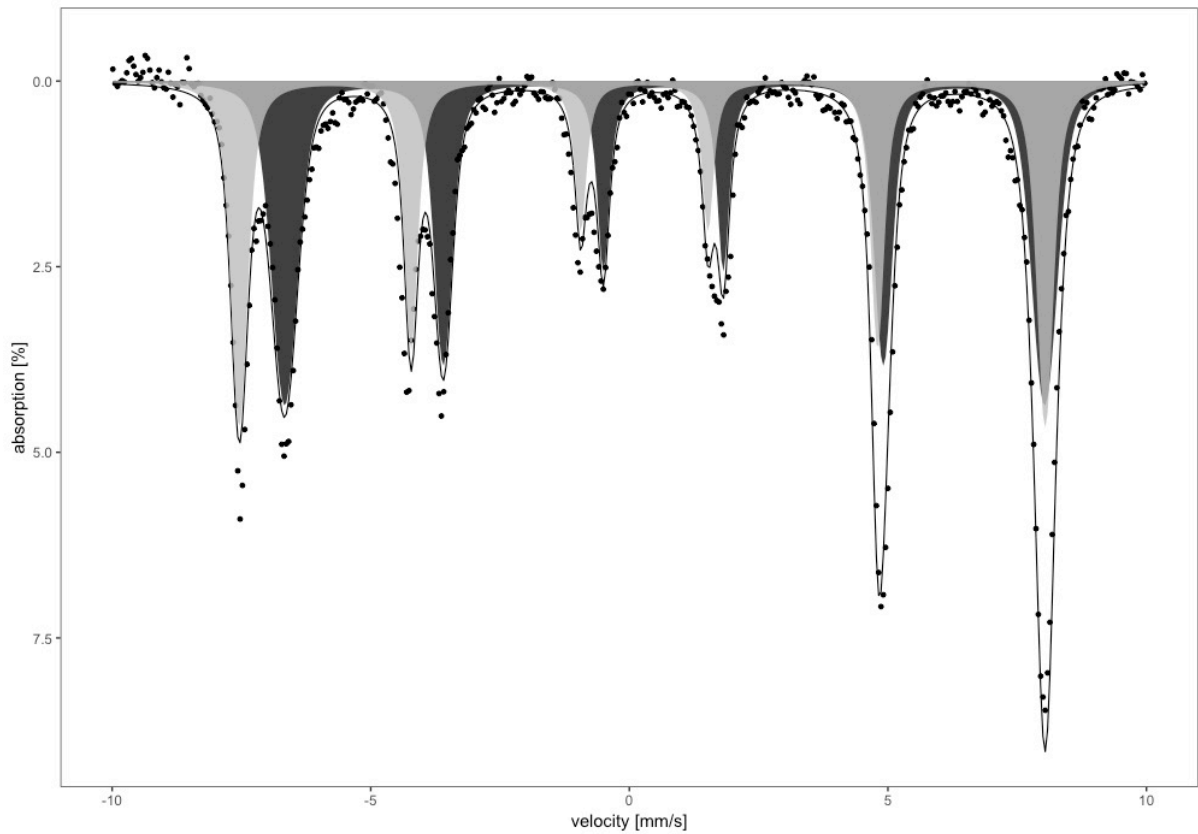
1206

1207 *Figure B10: Observed (black circles) and fitted (orange line) Mössbauer spectroscopy*
1208 *spectrum for the unleached synthetic goethite sample used in this study.*



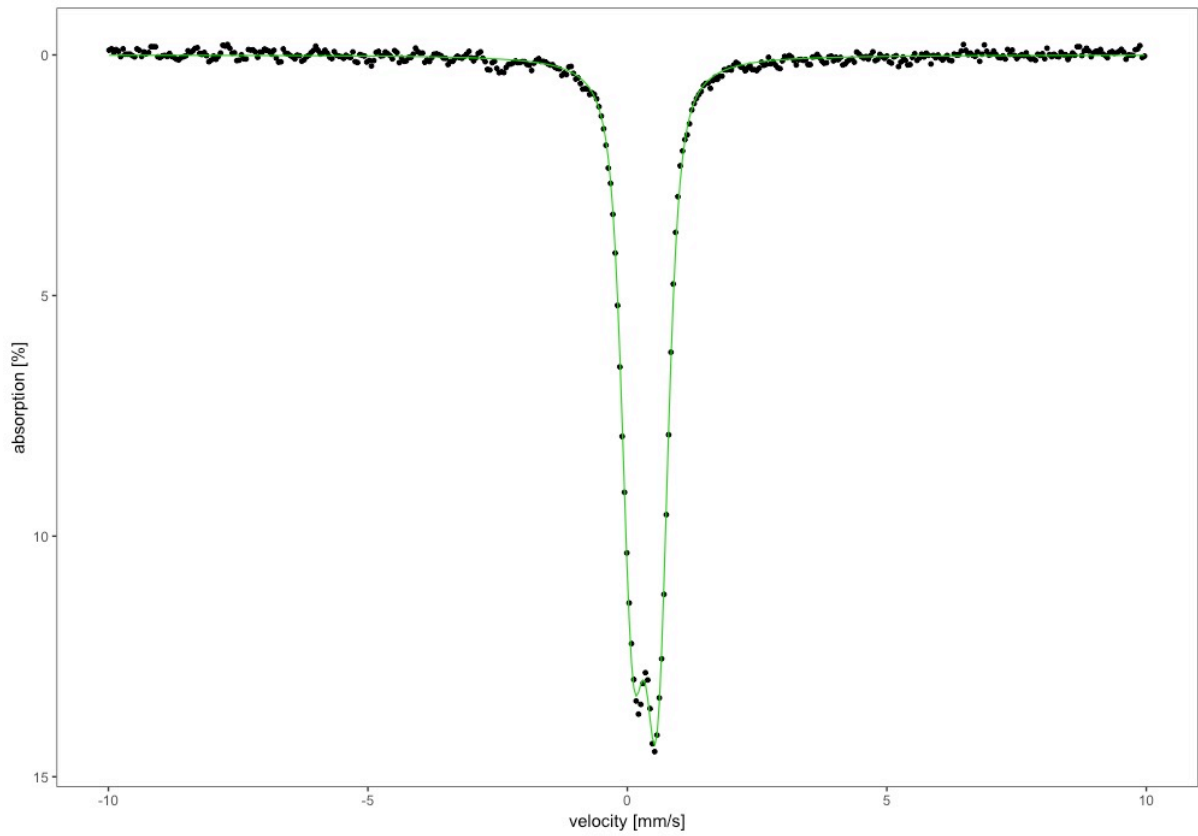
1209

1210 *Figure B11: Observed (black circles) and fitted (orange line) Mössbauer spectroscopy*
1211 *spectrum for the unleached natural UoE goethite sample used in this study.*



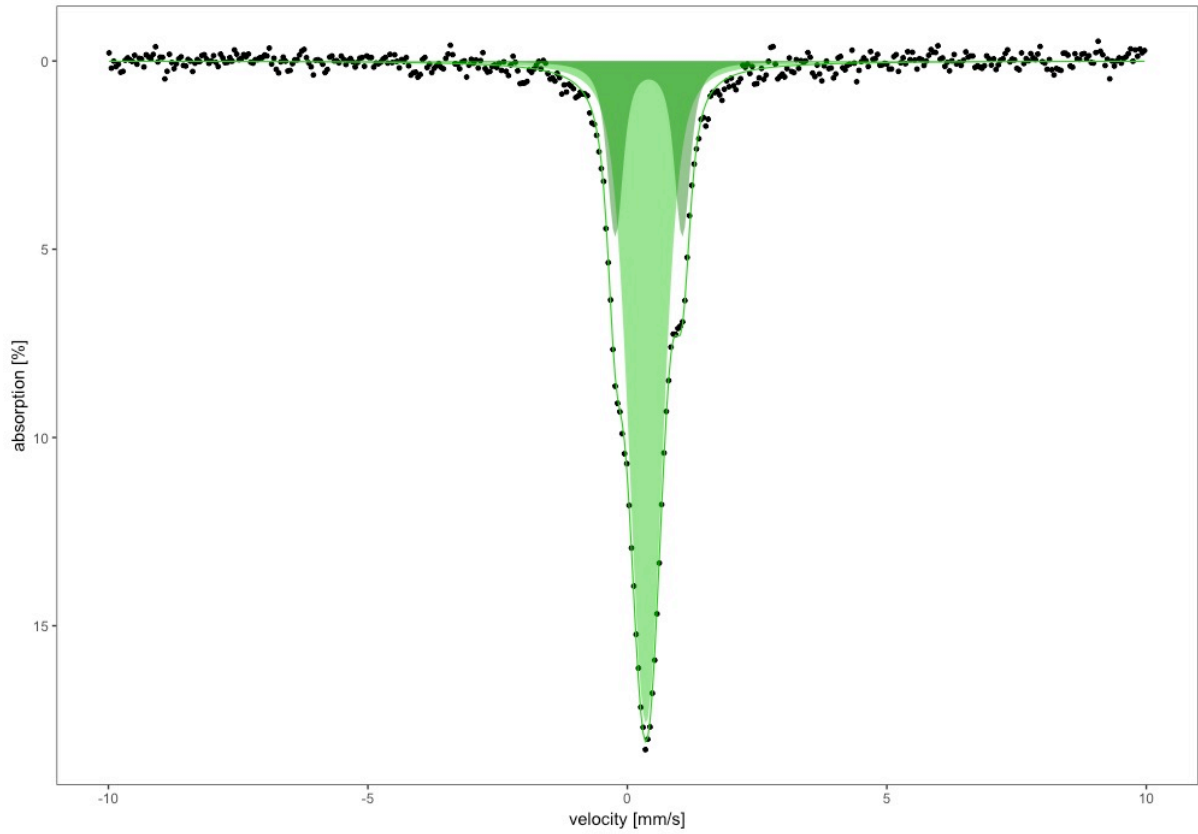
1212

1213 *Figure B12: Observed (black circles) and fitted (black line) Mössbauer spectroscopy spectrum for the*
 1214 *unleached synthetic magnetite sample used in this study. Magnetite is represented by two*
 1215 *subspectra. The black-filled area represents Fe³⁺ in tetrahedral crystal lattice sites. The grey-filled*
 1216 *area represents Fe²⁺ and Fe³⁺ in octahedral lattice sites with an average oxidation state of Fe^{2.5+}.*



1217

1218 *Figure B13: Observed (black circles) and fitted (green line) Mössbauer spectroscopy spectrum*
1219 *for the unleached natural NMS nontronite sample used in this study.*



1220

1221 *Figure B14: Observed (black circles) and fitted (green line) Mössbauer spectroscopy spectrum*
1222 *for the unleached natural NAu-2 nontronite sample used in this study. The Mössbauer*
1223 *parameters distinguish Fe³⁺ in a tetrahedral position in the crystal lattice (light green-filled*
1224 *area) from Fe³⁺ in an octahedral position (dark green-filled area).*

1225 **Appendix C to**

1226

1227 **The use of operationally-defined sequential Fe extraction methods**
1228 **for mineralogical applications: a cautionary tale from Mössbauer**
1229 **spectroscopy**

1230

1231 *Laura E. Hepburn, Ian B. Butler, Adrian Boyce, Christian Schröder*

1232

1233

1234 **Content**

1235

1236 **Table C1:** Mössbauer spectroscopy parameters for the individual Fe minerals unleached and
1237 following their target extraction stage only.

1238 **Table C2:** Mössbauer spectroscopy parameters for the individual Fe minerals unleached and at each
1239 stage of the sequential extraction until complete removal was observed.

1240 **Table C3:** Mössbauer spectroscopy parameters for the mixed Fe mineral sample CARB-2, unleached
1241 and after each stage of the sequential extraction between Fe_{aca-48} and Fe_{oxa}.

1242 **Table C4:** Mössbauer spectroscopy parameters for the mixed Fe mineral sample CARB-3, unleached
1243 and after each stage of the sequential extraction between Fe_{aca-48} and Fe_{HCl-1min}.

1244 **Table C1:** Mössbauer spectroscopy parameters for the individual Fe minerals unleached and
 1245 following their target extraction stage only. No data is shown for 2-line ferrihydrite since it was
 1246 completely removed during its target, Fe_{hyam} extraction. Parameters shown are Recoil compiled site
 1247 properties. δ = isomer shift; ΔE_Q = quadrupole splitting; B_{hf} = internal magnetic field; n = natural; s =
 1248 synthetic.

1249

Fe mineral	Ext. stage	Site	δ <i>mm/s</i>	ΔE_Q <i>mm/s</i>	B_{hf} <i>T</i>
Ivigtut siderite (<i>n</i>)	Fe _{UL}	Fe ²⁺	1.24	1.79	
		Fe ³⁺	0.39	-0.06	47.6
	Fe _{aca-48}	Fe ²⁺	1.24	1.78	
goethite (<i>s</i>)	Fe _{UL}	Fe ³⁺	0.33	-0.17	37.7
	Fe _{di-ct}	Fe ³⁺	0.51	-0.22	37.8
UoE goethite (<i>n</i>)	Fe _{UL}	Fe ³⁺	0.41	-0.12	31.3
	Fe _{di-ct}	Fe ³⁺	0.44	-0.07	32.3
magnetite (<i>s</i>)	Fe _{UL}	Fe ^{2.5+}	0.67	0.01	45.6
		Fe ³⁺	0.27	-0.02	48.3
	Fe _{oxa}	Fe ^{2.5+}	0.69	0.01	45.9
		Fe ³⁺	0.26	-0.03	48.4
NMS nontronite (<i>n</i>)	Fe _{UL}	Fe ³⁺	0.34	0.46	
	Fe _{HCl-1min}	Fe ³⁺	0.37	0.36	
NAu-2 nontronite (<i>n</i>)	Fe _{UL}	Fe ³⁺ (<i>tetra</i>)	0.36	0.10	
		Fe ³⁺ (<i>octa</i>)	0.41	1.3	
	Fe _{HCl-1min}	Fe ³⁺ (<i>tetra</i>)	0.37	0.00	

1250

1251 **Table C2:** Mössbauer spectroscopy parameters for the individual Fe minerals unleached and
 1252 at each stage of the sequential extraction until complete removal was observed. Parameters
 1253 shown are Recoil compiled site properties. δ = isomer shift; ΔE_Q = quadrupole splitting; B_{hf} =
 1254 internal magnetic field; n = natural; s = synthetic.

1255

Fe mineral	Ext. stage	Site	δ mm/s	ΔE_Q mm/s	B_{hf} T
Ivigtut siderite (n)	Fe _{UL}	Fe ²⁺	1.24	1.79	
		Fe ³⁺	0.39	-0.06	47.6
	Fe _{aca-48}	Fe ²⁺	1.24	1.78	
	Fe _{hyam}	Fe ²⁺	1.25	1.80	
	Fe _{di-ct}	Fe ²⁺	1.25	1.79	
	Fe _{oxa}	Fe ²⁺	1.25	1.79	
2-line ferrihydrite (s)	Fe _{UL}	Fe ²⁺	0.35	0.72	
	Fe _{aca-48}	Fe ²⁺	0.35	0.77	
goethite (s)	Fe _{UL}	Fe ³⁺	0.33	-0.17	37.7
	Fe _{aca-48}	Fe ³⁺	0.44	-0.08	37.6
	Fe _{hyam}	Fe ³⁺	0.39	-0.16	37.7
UoE goethite (n)	Fe _{UL}	Fe ³⁺	0.41	-0.12	31.3
	Fe _{aca-48}	Fe ³⁺	0.37	-0.12	31.8
	Fe _{hyam}	Fe ³⁺	0.34	-0.16	32.0
	Fe _{di-ct}	Fe ³⁺	0.38	-0.12	31.5
	Fe _{oxa}	Fe ³⁺	0.33	-0.17	31.3
	Fe _{HCl-1min}	Fe ³⁺	0.34	-0.16	31.0
magnetite (s)	Fe _{UL}	Fe ^{2.5+}	0.67	0.01	45.6
		Fe ³⁺	0.27	-0.02	48.3
	Fe _{aca-48}	Fe ^{2.5+}	0.69	0.02	46.1
		Fe ³⁺	0.25	-0.03	48.4

1256		Fe _{hyam}	Fe ^{2.5+}	0.69	0.02	46.1
1257			Fe ³⁺	0.26	-0.03	48.7
1258		Fe _{di-ct}	Fe ^{2.5+}	0.69	0.02	46.0
1259			Fe ³⁺	0.27	-0.03	48.6
1260						
1261	NMS nontronite (<i>n</i>)	Fe _{UL}	Fe ³⁺	0.34	0.46	
		Fe _{aca-48}	Fe ³⁺	0.33	0.48	
		Fe _{hyam}	Fe ³⁺	0.33	0.46	
		Fe _{di-ct}	Fe ³⁺	0.37	0.67	
		Fe _{oxa}	Fe ³⁺	0.21	0.67	
		Fe _{HCl-1min}	Fe ³⁺	0.28	0.00	
	NAu-2 nontronite (<i>n</i>)	Fe _{UL}	Fe ³⁺ (<i>tetra</i>)	0.36	0.10	
			Fe ³⁺ (<i>octa</i>)	0.41	1.3	
		Fe _{aca-48}	Fe ³⁺ (<i>tetra</i>)	0.38	0.00	
		Fe _{hyam}	Fe ³⁺ (<i>tetra</i>)	0.37	0.00	
		Fe _{di-ct}	Fe ³⁺ (<i>tetra</i>)	0.36	0.00	
		Fe _{oxa}	Fe ³⁺ (<i>tetra</i>)	0.38	0.00	
		Fe _{HCl-1min}	Fe ³⁺ (<i>tetra</i>)	0.36	0.00	

1262 **Table C3:** Mössbauer spectroscopy parameters for the mixed Fe mineral sample CARB-2,
 1263 unleached and after each stage of the sequential extraction between Fe_{aca-48} and Fe_{oxa}; all
 1264 trace of Fe was removed during the Fe_{HCl-1min} extraction. Parameters shown are Recoil
 1265 compiled site properties. δ = isomer shift; ΔE_Q = quadrupole splitting; B_{hf} = internal magnetic
 1266 field; n = natural; s = synthetic.

1267

Ext. stage	Fe mineral	Site	δ mm/s	ΔE_Q mm/s	B_{hf} T
CARB-2 Fe _{UL}	Ivigut siderite (n)	Fe ²⁺	1.24	1.79	
	2-line ferrihydrite (s)	Fe ²⁺	0.35	0.72	
	goethite (s)	Fe ³⁺	0.33	-0.17	37.7
	magnetite (s)	Fe ^{2.5+}	0.67	0.01	45.6
		Fe ³⁺	0.27	-0.02	48.3
	NMS nontronite (n)	Fe ³⁺	0.34	0.46	
CARB-2 Fe _{aca-48}	Ivigut siderite (n)	Fe ²⁺	1.24	1.79	
	2-line ferrihydrite (s)	Fe ²⁺	0.35	0.72	
	goethite (s)	Fe ³⁺	0.33	-0.17	37.7
	magnetite (s)	Fe ^{2.5+}	0.67	0.01	45.6
		Fe ³⁺	0.27	-0.02	48.3
	NMS nontronite (n)	Fe ³⁺	0.34	0.46	
CARB-2 Fe _{hyam}	Ivigut siderite (n)	Fe ²⁺	1.24	1.79	
	goethite (s)	Fe ³⁺	0.33	-0.17	37.7
	magnetite (s)	Fe ^{2.5+}	0.67	0.01	45.6
		Fe ³⁺	0.27	-0.02	48.3
	NMS nontronite (n)	Fe ³⁺	0.34	0.46	
	CARB-2 Fe _{di-ct}	Ivigut siderite (n)	Fe ²⁺	1.24	1.79
goethite (s)		Fe ³⁺	0.33	-0.17	37.7
magnetite (s)		Fe ^{2.5+}	0.67	0.01	45.6

		Fe ³⁺	0.27	-0.02	48.3
	NMS nontronite (<i>n</i>)	Fe ³⁺	0.34	0.46	
CARB-2 Fe _{oxa}	Iviglut siderite (<i>n</i>)	Fe ²⁺	1.24	1.79	
	goethite (<i>s</i>)	Fe ³⁺	0.33	-0.17	37.7

1268

1269 **Table C4:** Mössbauer spectroscopy parameters for the mixed Fe mineral sample CARB-3,
 1270 unleached and after each stage of the sequential extraction between Fe_{aca-48} and Fe_{HCl-1min};
 1271 all trace of Fe was removed during the final Fe_U extraction. Parameters shown are Recoil
 1272 compiled site properties. δ = isomer shift; ΔE_Q = quadrupole splitting; B_{hf} = internal magnetic
 1273 field; n = natural; s = synthetic.

1274

Ext. stage	Fe mineral	Site	δ mm/s	ΔE_Q mm/s	B_{hf} T
CARB-3 Fe _{UL}	Iviglut siderite (<i>n</i>)	Fe ²⁺	1.24	1.79	
	2-line ferrihydrite (<i>s</i>)	Fe ²⁺	0.35	0.72	
	UoE goethite (<i>n</i>)	Fe ³⁺	0.41	-0.12	31.3
	magnetite (<i>s</i>)	Fe ^{2.5+}	0.67	0.01	45.6
		Fe ³⁺	0.27	-0.02	48.3
	NAu-2 nontronite (<i>n</i>)	Fe ³⁺ (<i>tetra</i>)	0.36	0.12	
		Fe ³⁺ (<i>octa</i>)	0.41	0.16	
CARB-3 Fe _{aca-48}	Iviglut siderite (<i>n</i>)	Fe ²⁺	1.24	1.79	
	2-line ferrihydrite (<i>s</i>)	Fe ²⁺	0.35	0.72	
	UoE goethite (<i>n</i>)	Fe ³⁺	0.41	-0.12	31.3
	magnetite (<i>s</i>)	Fe ^{2.5+}	0.67	0.01	45.6
		Fe ³⁺	0.27	-0.02	48.3
	NAu-2 nontronite (<i>n</i>)	Fe ³⁺ (<i>tetra</i>)	0.36	0.12	
		Fe ³⁺ (<i>octa</i>)	0.41	0.16	
CARB-3 Fe _{hyam}	Iviglut siderite (<i>n</i>)	Fe ²⁺	1.24	1.79	
	UoE goethite (<i>n</i>)	Fe ³⁺	0.41	-0.12	31.3
	magnetite (<i>s</i>)	Fe ^{2.5+}	0.67	0.01	45.6
		Fe ³⁺	0.27	-0.02	48.3
	NAu-2 nontronite (<i>n</i>)	Fe ³⁺ (<i>tetra</i>)	0.36	0.12	
Fe ³⁺ (<i>octa</i>)		0.41	1.29		

CARB-3 Fe _{di-ct}	Ivigtut siderite (<i>n</i>)	Fe ²⁺	1.24	1.79	
	UoE goethite (<i>n</i>)	Fe ³⁺	0.41	-0.12	31.3
	magnetite (<i>s</i>)	Fe ^{2.5+}	0.67	0.01	45.6
		Fe ³⁺	0.27	-0.02	48.3
	NAu-2 nontronite (<i>n</i>)	Fe ³⁺ (<i>tetra</i>)	0.36	0.12	
CARB-3 Fe _{oxa}	Ivigtut siderite (<i>n</i>)	Fe ²⁺	1.24	1.79	
	UoE goethite (<i>n</i>)	Fe ³⁺	0.41	-0.12	31.3
	NAu-2 nontronite (<i>n</i>)	Fe ³⁺ (<i>tetra</i>)	0.36	0.12	
CARB-3 Fe _{HCl-1min}	Ivigtut siderite (<i>n</i>)	Fe ²⁺	1.24	1.79	
	NAu-2 nontronite (<i>n</i>)	Fe ³⁺ (<i>tetra</i>)	0.36	0.12	

1275

1276